



UNIVERSIDAD DE CONCEPCIÓN  
FACULTAD DE CIENCIAS FÍSICAS Y MATEMÁTICAS  
CIENCIAS FÍSICAS

VLASOV-POISSON SIMULATIONS OF THE  
TRANSVERSE INSTABILITY OF BGK-LIKE MODES IN  
BUMP-ON-TAIL DISTRIBUTED PLASMAS

Thesis presented in partial fulfillment of the requirements to receive the  
degree of Master of Science in Physics

Author: Jorge Abraham Gidi Chomalí  
Advisor: Dr. Jaime Andrés Araneda Sepúlveda  
Co-advisor: Dr. Roberto Elías Navarro Maldonado

August 31, 2020  
Concepción, Chile



# Agradecimientos

El mundo está lleno de personas maravillosas, y cada desafío en la vida es una oportunidad para descubrir la amabilidad de quienes te rodean.

Sobre todo en momentos como hoy, difícilmente podría haber logrado cumplir con este reto si no fuera por todo el apoyo que recibí, ya sea por parte de quienes físicamente me acompañan, como de quienes se han preocupado activamente de mi, aún a pesar de la distancia.

Aunque sería imposible nombrar a cada una de las personas que me ha apoyado, no puedo dejar de mencionar a la Familia Unida, que me sostiene en cada paso que doy; a mis amigos, quienes cada día me sorprenden con su bondad infinita; o a mis tutores, Jaime Araneda, con su vasta experiencia y comprensión, y Roberto Navarro, cuya calidad humana no tiene medida, y que además de ejemplo es un amigo.

Adicionalmente, agradezco el apoyo brindado por la Universidad de Concepción mediante la beca de Articulación Pregrado-Postgrado, y la Agencia Nacional de Investigación y Desarrollo, ANID Chile, mediante FONDECyt No. 1161700 (J.A.A.S.) y No. 11180947 (R.E.N.M.), CONYCyT-PAI No. 79170095 (R.E.N.M.), y la beca de Magíster No. 22182344 (J.A.G.C.).

*Спасибо, Александра!*

# Acknowledgments

The world is full of wonderful people, and every challenge in life is an opportunity to discover the kindness of the persons around you.

Especially at times like this, I couldn't have accomplished this challenge without all of the support received, be it from the ones who physically accompany me, or the ones actively interested in me, no matter the distance.

While it would be impossible to name all of the people who have supported me, I can't help to mention the *Familia Unida*, holding me at every step I make; my friends, who continue to astonish me with their infinite wholesomeness; or my advisors, Jaime Araneda, with his extensive experience and empathy, and Roberto Navarro, whose human quality is beyond all measure, and who besides an example to follow, has become a friend to me.

Additionally, I am thankful for the support given by the Universidad de Concepción through the Undergraduate-Postgraduate articulation scholarship, and the Agencia Nacional de Investigación y Desarrollo, ANID Chile, through FONDECyt No. 1161700 (J.A.A.S.) and No. 11180947 (R.E.N.M.), CONYCyT-PAI No. 79170095 (R.E.N.M.), and the Master's fellowship No. 22182344 (J.A.G.C.).

*Спасибо, Александра!*

*A quienes intentan hacer un mundo mejor para todos*



*To the people who try to make a better world for everyone*



# Contents

|          |   |          |
|----------|---|----------|
| <b>1</b> | <b>Introduction</b>                           | <b>3</b> |
| 1.1      | Problem statement . . . . .                   | 3        |
| 1.2      | Hypothesis . . . . .                          | 4        |
| 1.3      | Objectives . . . . .                          | 4        |
| 1.3.1    | General objective . . . . .                   | 4        |
| 1.3.2    | Specific objectives . . . . .                 | 5        |
| 1.4      | Methodology and organization . . . . .        | 5        |
| <b>2</b> | <b>Theoretical Framework</b>                  | <b>7</b> |
| 2.1      | Vlasov-Poisson system of equations . . . . .  | 7        |
| 2.2      | Waves in an unmagnetized plasma . . . . .     | 8        |
| 2.2.1    | Linear theory . . . . .                       | 8        |
| 2.2.2    | Trapping and BGK modes . . . . .              | 13       |
| 2.2.3    | Transverse instability of BGK modes . . . . . | 17       |
| 2.3      | Vlasov-Poisson Simulations . . . . .          | 18       |
| 2.3.1    | Dimensionless system of equations . . . . .   | 21       |
| 2.3.2    | Symplectic interators . . . . .               | 22       |
| 2.3.3    | Solution of the advection equations . . . . . | 25       |
| 2.3.4    | Electrostatic force calculation . . . . .     | 26       |
| 2.3.5    | Validity of the simulations . . . . .         | 27       |

|          |  |           |
|----------|--|-----------|
| <b>3</b> | <b>Results and Discussion</b>  | <b>28</b> |
| 3.1      | Numerical setup . . . . .  | 28        |
| 3.2      | Results . . . . .  | 31        |
| 3.2.1    | Description of the instability . . . . .                                 | 31        |
| 3.2.2    | Analysis of the transverse growth rates . . . . .                        | 37        |
| <b>4</b> | <b>Conclusions</b>   | <b>43</b> |
|          | <b>Appendix</b>  | <b>45</b> |
| <b>A</b> | <b>Conventions</b>   | <b>45</b> |
| A.1      | Characteristic quantities . . . . .                                      | 45        |
| A.2      | Gradient with respect to a vector . . . . .                              | 46        |
| A.3      | Fourier transform . . . . .  | 47        |
| <b>B</b> | <b>Analytical Calculations</b>   | <b>48</b> |
| B.1      | Electrostatic dispersion relation for a Maxwellian equilibrium . . . . . | 48        |
|          | <b>Bibliography</b>  | <b>51</b> |





# List of Figures

|     |   |    |
|-----|---|----|
| 2.1 | Real (a) and imaginary (b) parts of the complex frequency, $\omega$ , as a function of the wavenumber, $k$ , allowed on Maxwellian electron plasma according to the linear dispersion relation (2.10). Black lines are Langmuir branches and gray lines are pseudo-acoustic branches. $\omega_{pe}$ and $v_{te}$ are the plasma frequency and the thermal speed of electronic plasma, respectively. . . . . | 11 |
| 2.2 | Real (a) and imaginary (b) parts of the complex frequency, $\omega$ , as a function of the wavenumber, $k$ , on a bump-on-tail electron plasma according to the linear dispersion relation (2.10). Black lines are Langmuir branches and gray lines are pseudo-acoustic branches. $\omega_{pe}$ and $v_{te}$ are the plasma frequency and the thermal speed of electronic plasma, respectively. . . . .     | 12 |
| 2.3 | Constant contours of the single-particle energy, $W'$ , in the frame of reference of the wave. The red contour marks the separatrix between the free-streaming ( $W' > 0$ , white background) and trapping ( $W' < 0$ , gray shade) regions. . . . .  | 14 |

|     |   |    |
|-----|---|----|
| 2.4 | Illustration of a Maxwellian equilibrium distribution function (black solid line) and the formation of a <i>plateau</i> (black dashed line) due to nonlinear interaction with a wave $(\omega_r, k)$ . The red vertical line marks the phase velocity of the wave and the gray shade marks the trapping region. . . . .   | 15 |
| 3.1 | Maximum growth rates scanned from the linear dispersion relation (2.10), as a function of the wavevector, $\mathbf{k} = (k_x, k_y)$ , for a beam with density of 10% ( $\varepsilon = 0.1$ ) and a drift $V_d/v_{te} = 3$ . The white diamond marks the most unstable configuration and the gray dashed line follows the highest growth rate for each value of $k_y$ . Only growth rates, $\gamma/\omega_{pe} > 10^{-3}$ are shown. . . . .   | 30 |
| 3.2 | Spectral decomposition of the electrostatic energy. On the bottom panel, (b), the energy of the perturbed mode, $(k_0, 0)$ (in red), and its first 15 transverse harmonics, $(k_0, k_y)$ (from purple to black, as $k_y$ gets larger), on a 2-dimensional simulation with $\varepsilon = 0.1$ and $V_d/v_{te} = 3$ . Gray dotted lines stand for the growth rates predicted from the linear dispersion relation (2.10). On top, (a), the energy of the perturbed mode, $k = k_0$ on an equivalent simulation restricted to 1-dimensional evolution. White arrows mark the instants shown on the phase-space panels of Fig. 3.3. On both panels a logarithmic scale is used for the vertical axis, and gray/white backgrounds mark different stages during the evolution of the systems. . . . . | 32 |

- 3.3 Phase-space vortex formed in 1– and 2–dimensional simulations with  $\varepsilon = 0.1$  and  $V_d/v_{te} = 3$ . The four panels on top, (a) to (f), correspond to the electron distribution function on a 1–dimensional simulation, and the four panels on the bottom, (e) to (h), to the transverse-averaged electron distribution function,  $\langle f_e \rangle(x, v_x)$ , on a 2–dimensional simulation. Times  $t_1$  to  $t_4$  correspond to the white arrows on Fig. 3.2. Yellow/black color stands for a higher/lower density of electrons. The colorscale is logarithmic, and its limits have been restricted to show only levels relevant to the vortex. . . . . 34
- 3.4 Velocity profile of the averaged electron distribution function,  $\langle f_e \rangle(v_x, v_y)$  on a simulation with  $\varepsilon = 0.1$  and  $V_d/v_{te} = 3$ . The bottom panels (d), (e) and (f) show contour lines of the distribution, and the top panels (a), (b) and (c), cuts of for  $v_y/v_{te} = 0$  (blue),  $v_y/v_{te} = 0.5$  (red) and  $v_y/v_{te} = 1$  (green). Three instants are shown: (a) and (d) at the start of the simulation  $t\omega_{pe} = 0$  on stage I; (b) and (e) when the BGK-like mode parallel to the beam dominates on stage II  $t\omega_{pe} = 700$ ; and (c) and (f) after the transverse collapse on stage IV  $t\omega_{pe} = 1500$ . The dashed colored lines in the bottom panels mark the velocity cuts shown with the same colors in the panels above. . . . . 35

- 3.5 Power spectrum of the averaged electron charge density for a 2-dimensional simulation with  $\varepsilon = 0.1$  and  $V_d/v_{te} = 3$ . Upper panels (a), (b), and (c), show the power spectrum parallel to the beam,  $(\omega, k_x)$ . Bottom panels, (d), (e), and (f), the power spectrum transverse to the beam,  $(\omega, k_y)$ . Three time ranges are shown: (a) and (d) during stage I, (b) and (e) during stage II, and (c) and (f) during stage IV. The solid vertical lines mark  $\omega_r = 0$  and the dashed vertical lines mark  $\omega_0/\omega_{pe} = 0.695$ , the frequency predicted from linear theory for the mode initially excited  $(k_x, k_y) = (k_0, 0)$ . The colorscale is logarithmic and it has been normalized against the maximum power for each case, which is: (a)  $8 \cdot 10^7$ , (b)  $3 \cdot 10^{10}$ , (c)  $3 \cdot 10^8$ , (d)  $5 \cdot 10^{-18}$ , (e)  $2 \cdot 10^{-7}$ , and (f)  $2 \cdot 10^2$ . . . . . 36
- 3.6 Transverse growth rates as a function of the transverse wavenumber,  $k_y$ . Beam density  $\varepsilon = 0.1$ . Lines of different colors are simulations with different initial drift velocity,  $V_d$ . White diamonds mark the maximum transverse growth rate,  $\gamma_m$ , and the red line is a quadratic fit for  $V_d/v_{te} \leq 4.5$ ,  $\gamma_m(k_y) = 0.392k_y + 4.938k_y^2$ . . . . . 38
- 3.7 Maximum transverse growth rate,  $\gamma_m$ , as a function of the transverse wavenumber,  $k_y$ . Each diamond is an individual simulation. Colors red, blue and green stand for  $\varepsilon = 0.05$ ,  $\varepsilon = 0.1$  and  $\varepsilon = 0.2$ , respectively. Solid lines are quadratic fits for  $V_d/v_{te} \leq 4.5$  for each group of simulations: in red  $\gamma_m^{\varepsilon=0.05}(k_y) = 0.254k_y + 4.439k_y^2$ , in blue  $\gamma_m^{\varepsilon=0.1}(k_y) = 0.392k_y + 4.938k_y^2$ , and in green  $\gamma_m^{\varepsilon=0.2}(k_y) = 0.605k_y + 3.564k_y^2$ . . . . . 39

3.8 Transverse growth rates as a function of the relative drift velocity,  $V_d$ , for simulations with  $\varepsilon = 0.05$  (red),  $\varepsilon = 0.1$  (blue), and  $\varepsilon = 0.2$  (green). Diamonds mark the maximum transverse growth rate,  $\gamma_m$ , measured for oblique modes with parallel wavenumber  $k_0$ , after the nonlinear saturation of the perturbed mode  $(k_0, 0)$ . Solid lines are quadratic fits: in red  $\gamma(V_d) = 0.046(V_d - V_{th}^{\varepsilon=0.05}) - 0.01(V_d - V_{th}^{\varepsilon=0.05})^2$ , in blue  $\gamma(V_d) = 0.067(V_d - V_{th}^{\varepsilon=0.1}) - 0.014(V_d - V_{th}^{\varepsilon=0.1})^2$ , and in green  $\gamma(V_d) = 0.073(V_d - V_{th}^{\varepsilon=0.2}) - 0.011(V_d - V_{th}^{\varepsilon=0.2})^2$ . Circles mark the growth rate of the same modes during the linear stage, obtained from linear theory, and the dashed lines are quadratic fits. Stars on the horizontal axis mark the linear instability thresholds,  $V_{th}^{\varepsilon=0.05}/v_{te} = 2.82$ ,  $V_{th}^{\varepsilon=0.1}/v_{te} = 1.97$ , and  $V_{th}^{\varepsilon=0.2}/v_{te} = 2.42$  for the initial bump-on-tail configuration. . . . . 41

3.9 Maximum transverse growth rates,  $\gamma_m$ , as a function of the linear growth rate of the mode initially excited,  $\gamma_L$ , obtained from the linear dispersion relation. Each diamond is a different simulation. Red, blue and green colors mark configurations with  $\varepsilon = 0.05$ ,  $\varepsilon = 0.1$ , and  $\varepsilon = 0.2$ , respectively. Solid lines are: in red  $\gamma_m^{\varepsilon=0.05}(\gamma_L) = 0.309\gamma_L$ , in blue  $\gamma_m^{\varepsilon=0.1}(\gamma_L) = 0.404\gamma_L$ , and in green  $\gamma_m^{\varepsilon=0.2}(\gamma_L) = 0.456\gamma_L$ . . . . . 42

# Resumen

Se utilizan simulaciones directas del sistema de Vlasov-Poisson en 2 dimensiones espaciales para estudiar la formación e inestabilidad transversal de modos tipo BGK originados por interacción auto-consistente en plasmas con distribuciones bump-on-tail.

La configuración de bump-on-tail excita modos paralelos y oblicuos al *beam* de manera consistente con predicciones de teoría lineal. Al ser formado un modo tipo BGK, las tasas de crecimiento de los modos oblicuos son modificadas, y siguen relaciones sencillas con respecto a la inestabilidad original de bump-on-tail.

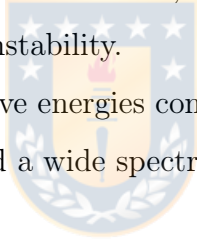
Cuando los modos oblicuos alcanzan energías comparables a la energía del modo tipo BGK, este último colapsa, y un amplio espectro de armónicos transversales es saturado.

# Abstract

Direct simulations of the Vlasov-Poisson system of equations in 2 physical dimensions are used to study the formation and transverse instability of BGK-like modes originated from self-consistent interaction in bump-on-tail distributed plasmas.

The bump-on-tail configuration excites modes parallel and oblique to the beam, consistent with predictions from linear theory. Once a BGK-like mode is formed, the growth rates of oblique modes are modified, and follow simple relations with respect to the original bump-on-tail instability.

When oblique modes achieve energies comparable to the energy of the BGK-like mode, the latter collapses, and a wide spectrum of transverse harmonics saturate.



# Planteamiento del problema

Un plasma no-colisional puede ser modelado en la aproximación electrostática por medio del sistema de ecuaciones de Vlasov-Poisson, el cual admite un tipo de soluciones exactas, no lineales, llamadas modos Bernstein-Greene-Kruskal (BGK) [1].

Modos tipo BGK son recurrentemente observados en plasmas espaciales [2] y de laboratorio [3], y aún cuando múltiples simulaciones 1–dimensionales han mostrado que estos se asocian a estructuras estables, y que representan estados asintóticos de plasmas con distribuciones de velocidad inestables [4] o distribuciones estables sujetas a perturbaciones no-lineales [5], simulaciones PIC no-magnetizadas en múltiples dimensiones han mostrado por un largo tiempo que un tipo de modo BGK localizado llamado *electron hole* [6] se rompe cuando el sistema puede evolucionar a lo largo de una dimensión transversal al *trapping* del modo [7]. Este fenómeno ha sido denominado inestabilidad transversal, y es sabido que afecta también a otros modos de tipo BGK. Por ejemplo, se ha desarrollado teorías para explicar la filamentación de ondas de Langmuir de amplitud finita [8, 9], y aunque simulaciones PIC coinciden cualitativamente con ellas [10], simulaciones de Vlasov con menor ruido han revelado la necesidad de refinar las teorías actuales [11]. De la misma manera, simulaciones de Vlasov han verificado la inestabilidad transversal de ondas Ion Acústicas, pero las tasas de crecimiento asociadas a esta no han podido ser explicadas [12].

A la luz de la evidencia presentada, es claro que las simulaciones de Vlasov mantienen un rol clave en cuanto a proveer evidencia de la inestabilidad transversal de modos BGK, contribuyendo al perfeccionamiento de las teorías actuales, y a la



comprensión de los mecanismos físicos de la inestabilidad.

Dado que los estudios modernos de la inestabilidad transversal de modos BGK se basan en simulaciones numéricas de modos tipo BGK formados por bombeo mediante un potencial externo [9], o simulaciones configuradas a partir de modelos analíticos [11], este trabajo busca proveer evidencia adicional en torno al fenómeno al utilizar simulaciones de Vlasov para estudiar la inestabilidad transversal de modos tipo BGK formados auto-consistentemente a partir de distribuciones inestables de bump-on-tail, las cuales corresponden a uno de los orígenes más comunes y sencillos de los modos de tipo BGK.



# Chapter 1

## Introduction

### 1.1 Problem statement

A collisionless plasma may be modelled in the electrostatic approximation by means of the Vlasov-Poisson system of equations, which admits a kind of exact, nonlinear solutions called Bernstein-Greene-Kruskal (BGK) modes [1].

BGK-like modes are continuously observed in space [2] and laboratory plasmas [3], and while multiple 1–dimensional simulations have portrayed them as stable structures arising as the asymptotic state from unstable velocity distributions [4] or nonlinear perturbations to stable distributions [5], unmagnetized PIC simulations in multiple dimensions have long shown that electron holes, a localized kind of BGK mode [6], break up when the system is allowed to evolve transverse to their trapping direction [7]. This phenomenon has been called *transverse instability*, and it is known to affect other kinds of BGK-like modes. For example, a theory for the filamentation of Large Amplitude Langmuir Waves has been developed [8, 9] and PIC simulations show qualitative agreement [10], but cleaner Vlasov simulations show the need to improve current theories [11]. Similarly, Vlasov simulations attest for the transverse instability of Ion Acoustic Waves, but the growth rates measured are yet to be explained [12].

In the light of the aforementioned evidence, Vlasov simulations still have a key role in providing further evidence on the transverse instability of BGK modes, thus allowing the improvement of current theories and leading to a better understanding on its physical mechanisms.

Since modern studies on the transverse instability of BGK modes are based on numerical simulations of BGK-like modes formed by pumping of an external driver [9], or simulations initialized from analytical models [11], this work aims to provide further evidence by using Vlasov simulations to study the transverse instability of BGK-like modes self-consistently formed from unstable bump-on-tail distributions, which is one of the simplest and most common kind of origin for a BGK-like mode.

## 1.2 Hypothesis

BGK-like modes formed from self-consistent interactions in electrostatic bump-on-tail distributed plasmas are unstable to perturbations transverse to its trapping direction, and the instability can be closely related to the unstable phase-space distribution which generated the BGK-like mode.

## 1.3 Objectives

### 1.3.1 General objective

To study the transverse stability of BGK-like modes formed from unstable bump-on-tail distributions in electrostatic plasmas, relating the development of the instability to the initial phase-space distribution.

### 1.3.2 Specific objectives

- To implement a Vlasov-Poisson code allowing to simulate the evolution of unmagnetized electrostatic plasmas in 1 and 2 physical dimensions.
- To form BGK-like states from the self-consistent evolution of linearly unstable velocity distributions in 1– and 2–dimensional simulations.
- To characterize the evolution of the unstable distributions in 1 and 2 physical dimensions.
- To measure the transverse growth rates and to identify thresholds for the transverse instability of the BGK-like modes in 2 physical dimensions.
- To relate the instability of the BGK-like modes in 2 physical dimensions with the bump-on-tail distributions which originated the BGK-like modes.

## 1.4 Methodology and organization

A computational library will be written to directly solve the Vlasov-Poisson system of equations in 1 and 2 physical dimensions, using periodic boundary conditions, splitting of the Vlasov equation, spectral interpolation and symplectic integration in a backwards semi-Lagrangian scheme.

This library will be written in the Julia programming language [13], which is registered under the open source MIT licence. Julia is a high-level, high-performance, interactive language, and its ecosystem is wide enough to facilitate the implementation of the simulations required, as much as the analysis of the results with relative ease.

The aforementioned library will run on a server with 512 Gb of RAM and two processors Intel Xeon E5-2699V4 of 44 threads each, running at 2.2 GHz. The

operative system of the server is Debian GNU/Linux 10 (buster) with kernel 4.19.0-6-amd64, and the official binaries of the Julia language, version 1.4.1, will be used.

The formation of BGK-like modes will be induced in a self-consistent manner by means of linearly unstable bump-on-tail velocity configurations in 2–dimensional simulations, and the instability of the mode towards the excitation of transverse harmonics will be analyzed.

By use of the Vlasov-Poisson model, the validity of the results are restricted to collisionless plasmas where the electrostatic approximation is valid. Also, background magnetic fields are neglected. While this study points towards the understanding of basic plasma-wave processes, there exist real-life scenarios close to this regime. Some examples are the ionosphere of celestial bodies with weak magnetic fields, such as Venus or Titan, or plasmas induced by laser ablation, with numerous applications in industry and medicine, like spectroscopy.

The document is organized in the following manner: In Chapter 2, the Vlasov-Poisson model will be introduced along with basic concepts from linear kinetic theory, like Landau damping and the bump-on-tail instability. A brief description is provided on the nonlinear effect of particle trapping, on how it gives rise to the existence of BGK modes, and the fact that they are unstable in multiple dimensions. Additionally, the foundations for the construction of numerical methods to solve the Vlasov-Poisson system of equations will be presented. In Chapter 3 the results from the numerical simulations will be presented. The transverse instability will be characterized and simple relations will be shown to exist between the transverse growth rates around a BGK-like mode, and the initial distribution which originated the mode. Finally, Chapter 4 summarizes the results of the numerical simulations, and how they respond to the hypothesis of work.

# Chapter 2

## Theoretical Framework

### 2.1 Vlasov-Poisson system of equations

Born from the kinetic theory, the Vlasov equation is a conservation equation which gives a statistical description to a collection of particles with no direct interaction. Each particle may only interact with fields induced collectively by the whole system.

Proposed by Anatoli Vlasov in a pioneering study of the vibrational properties of an electron gas in 1937 [14], this equation is sometimes referred to as the collisionless Boltzmann equation, and poses the evolution for each particle species as

$$\frac{\partial f_j}{\partial t} + \mathbf{v} \cdot \frac{\partial f_j}{\partial \mathbf{x}} + \mathbf{F}_j \cdot \frac{\partial f_j}{\partial \mathbf{v}} = 0, \quad (2.1)$$

where  $f_j = f_j(\mathbf{x}, \mathbf{v}, t)$  is the phase-space distribution function for the species  $j$ , subject to the conservative force  $\mathbf{F}_j$ .

To model the electrostatic evolution of unmagnetized plasmas, this document will make use of the Vlasov-Poisson system of equations without background magnetic field, meaning that the forcing term,  $\mathbf{F}_j$ , will be given by the Lorentz force,

$$\mathbf{F}_j = \frac{q_j}{m_j} \mathbf{E}, \quad (2.2)$$

where  $q_j$  and  $m_j$  are the charge and mass of the species  $j$ , respectively, and  $\mathbf{E} = \mathbf{E}(\mathbf{x}, t)$  is the electric field, self-consistently fixed according to the Faraday's law (2.3)

without magnetic induction and the Gauss's law (2.4), respectively,

$$\nabla \times \mathbf{E} = 0, \quad (2.3)$$

$$\nabla \cdot \mathbf{E} = 4\pi\rho, \quad (2.4)$$

with the total charge density,  $\rho = \rho(\mathbf{x}, t)$ , given by

$$\rho = \sum_j q_j \int_{\mathbb{R}^3} f_j d^3v. \quad (2.5)$$

## 2.2 Waves in an unmagnetized plasma

### 2.2.1 Linear theory

If we assume the plasma state to be separable into an homogeneous equilibrium, and small deviations,

$$f_j(\mathbf{x}, \mathbf{v}, t) = n_j f_j^0(\mathbf{v}) + \delta f_j(\mathbf{x}, \mathbf{v}, t), \quad (2.6)$$

$$\mathbf{E}(\mathbf{x}, t) = \delta \mathbf{E}(\mathbf{x}, t), \quad (2.7)$$

where  $n_j$  is the density of the species  $j$ , and the equilibrium distribution functions,  $f_j^0$ , fulfill the *quasineutrality* condition,

$$\rho^0 = \sum_j q_j \int_{\mathbb{R}^3} f_j^0 d^3v = 0, \quad (2.8)$$

the Vlasov-Poisson system of equations (2.1)-(2.5), can be linearized to obtain the linear dispersion relation [15],

$$1 + \sum_j \frac{\omega_{pj}^2}{|\mathbf{k}|^2} \int_{\mathbb{R}^3} \frac{\mathbf{k}}{\omega - \mathbf{k} \cdot \mathbf{v}} \cdot \frac{\partial f_j^0}{\partial \mathbf{v}} d^3v = 0, \quad (2.9)$$

where  $\omega_{pj} = \sqrt{4\pi n_j q_j^2 / m_j}$  is the plasma frequency of the species  $j$ , and  $\omega$  and  $\mathbf{k}$  are the frequency and wavevector of the perturbations propagating in the plasma, respectively.

At this point it is interesting to recall that the last integral is singular for  $\omega = \mathbf{k} \cdot \mathbf{v}$ , and it is therefore ill-defined if both the frequency,  $\omega$ , and the wavevector,  $\mathbf{k}$ , are demanded to be real-valued. This apparent dead-end brought problems to Vlasov [14], who first made this calculations and interpreted the integral in the sense of the principal value, but the situation was successfully tackled 8 years later by Landau [16], considering the resolution of the Vlasov equation as an initial value problem.

In practice, one usually considers a real-valued wavevector,  $\mathbf{k}$ , and the frequency  $\omega$  to be a complex scalar,

$$\omega = \omega_r + i\gamma,$$

where  $\omega_r$  is the oscillation frequency, and  $\gamma$  is the exponential growth rate of the wave.

It is very common to consider the equilibrium distribution function to be composed of Maxwellian contributions,

$$f_j^0 = \frac{1}{(2\pi)^{3/2} v_{tj}^3} \exp \left[ -\frac{(\mathbf{v} - \mathbf{V}_j)^2}{2v_{tj}^2} \right],$$

allowing to rewrite the dispersion relation (2.9) as<sup>1</sup>

$$1 - \sum_j \frac{\omega_{pj}^2}{2v_{tj}^2 |\mathbf{k}|^2} Z' \left( \frac{\omega - \mathbf{k} \cdot \mathbf{V}_j}{\sqrt{2}v_{tj}|\mathbf{k}|} \right) = 0, \quad (2.10)$$

where  $\mathbf{V}_j$ ,  $v_{tj} = \sqrt{k_B T_j / m_j}$ , and  $T_j$  are the drift velocity, thermal speed, and temperature of the species  $j$ , respectively, and  $k_B \approx 6.381[\text{erg} \cdot \text{K}^{-1}]$  is the Boltzmann's constant.  $\xi_j = (\omega - \mathbf{k} \cdot \mathbf{V}_j) / \sqrt{2}v_{tj}|\mathbf{k}|$  is called the *resonance factor* of the species  $j$ ,  $Z(\xi)$  is the *plasma dispersion function* from Fried and Conte [17],

$$Z(\xi) = \frac{1}{\sqrt{\pi}} \int_{\mathbb{R}} \frac{e^{-t^2}}{t - \xi} dt,$$

and  $Z'(\xi)$  denotes its first derivative.

---

<sup>1</sup>Proof: B.1 on page 48



### Maxwellian equilibrium

For an electron-proton plasma it is possible to use the approximation of *massive ions*, that is, to neglect the dynamics of the protons on the time scale of the electrons due to the high mass ratio between this two species, and consider protons merely as a static, neutralizing background. Under this approximation, and taking the electrons to follow a Maxwellian distribution function,

$$f_e(v) = \frac{1}{(2\pi)^{3/2}v_{te}^3} \exp\left(-\frac{v^2}{2v_{te}^2}\right),$$

the linear dispersion relation yields

$$\frac{\omega_{pe}^2}{2v_{te}^2k^2} Z'\left(\frac{\omega}{\sqrt{2}v_{te}k}\right) = 1, \quad (2.11)$$

where  $v_{te}$  and  $\omega_{pe}$  are the thermal speed of the electrons and the frequency of the electronic plasma, respectively.

Taking  $k$  as the real, independent variable, then equation (2.11) presents a number of complex solutions  $\omega = \omega(k)$ . Some of this solutions are shown on Fig. 2.1.

From Fig. 2.1a, the existence of two kinds of solutions can be distinguished:

- (i) Branches passing through the origin, with approximately constant phase velocity,  $v_\phi = \omega_r/k$ . This family of solutions are called *pseudo-acoustic* waves, due to the similarity of their shapes with the solutions of the dispersion relation of acoustic waves. From Fig. 2.1b it is observed that pseudo-acoustic modes are highly damped for all wavenumbers.
- (ii) Branches passing through the frequency axis at  $\pm\omega_{pe}$ , corresponding to Langmuir waves. This modes are approximately undamped for  $k \ll 1$ .

In no case a positive growth rate,  $\gamma > 0$ , can be found when the system is under a Maxwellian equilibrium without additional currents.

The damping of the perturbations allowed to propagate through the plasma is called *Landau damping*, as it was analytically found by Lev Landau in 1946 [16].

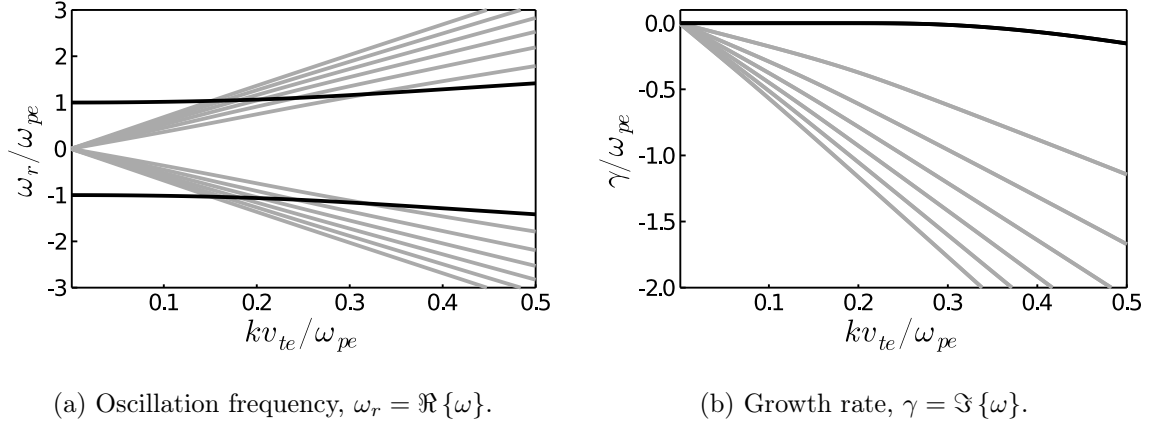


Figure 2.1: Real (a) and imaginary (b) parts of the complex frequency,  $\omega$ , as a function of the wavenumber,  $k$ , allowed on Maxwellian electron plasma according to the linear dispersion relation (2.10). Black lines are Langmuir branches and gray lines are pseudo-acoustic branches.  $\omega_{pe}$  and  $v_{te}$  are the plasma frequency and the thermal speed of electronic plasma, respectively.

Besides the obvious importance of the Landau damping in the study of plasmas, it has a very significant role in physics, posing that purely conservative interactions may result in wave damping and give rise to stability regions in the parameter space.

### Bump-on-tail equilibrium

It is possible to incorporate an electron beam to the previous Maxwellian equilibrium to obtain a bump-on-tail configuration,

$$f_e = \frac{1 - \epsilon}{(2\pi)^{3/2} v_{te}^3} \exp\left(-\frac{v^2}{2v_{te}^2}\right) + \frac{\epsilon}{(2\pi)^{3/2} v_{tb}^3} \exp\left(-\frac{(v - V_b)^2}{2v_{tb}^2}\right),$$

where  $\epsilon$  controls the intensity of the beam,  $v_{tb}$  is its thermal speed and  $V_b$  is its drift velocity. Introducing the bump-on-tail distribution function into the dispersion relation (2.10) yields

$$(1 - \epsilon) \frac{\omega_{pe}^2}{2v_{te}^2 k} Z'\left(\frac{\omega}{\sqrt{2}v_{te}k}\right) + \epsilon \frac{\omega_{pe}^2}{2v_{tb}^2 k^2} Z'\left(\frac{\omega - kV_b}{\sqrt{2}v_{tb}k}\right) = 1 \quad (2.12)$$

Just like the former case, there exists complex solutions  $\omega = \omega(k)$  to the equation (2.12), which are shown in Fig. 2.2 considering  $v_{tb} = v_{te}$  and  $V_b = 5v_{te}$ .

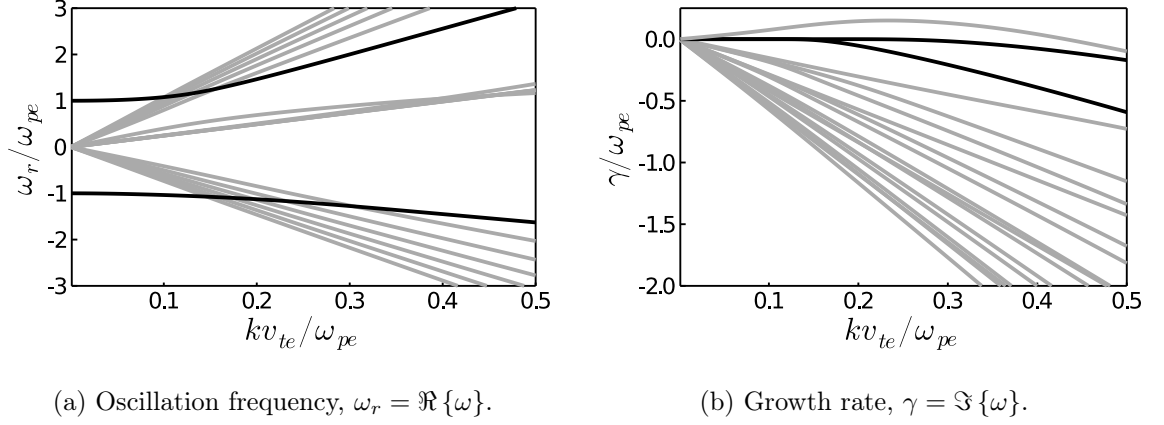


Figure 2.2: Real (a) and imaginary (b) parts of the complex frequency,  $\omega$ , as a function of the wavenumber,  $k$ , on a bump-on-tail electron plasma according to the linear dispersion relation (2.10). Black lines are Langmuir branches and gray lines are pseudo-acoustic branches.  $\omega_{pe}$  and  $v_{te}$  are the plasma frequency and the thermal speed of electronic plasma, respectively.

On Fig.2.2a the same kinds of solutions are observed compared to Fig.2.1a, but with a clear loss of symmetry around  $\omega_r = 0$  due to the presence of the beam. Fig. 2.2b shows a pseudo-acoustic branch with positive growth rate for a certain range of wavenumbers. This means that the presence of the beam provides free energy that may render some solutions unstable. This phenomenon is called the *bump-on-tail* instability, and predicts an exponential growth of the wave amplitude.

From linear theory it is known that the factors defining the stability of an electrostatic perturbation are its phase velocity,  $v_\phi = \omega_r/k$ , and the slope of the distribution function at that velocity,  $\left. \frac{\partial f}{\partial v} \right|_{v=\omega_r/k}$ . In fact, making use of the slow instability condition,  $|\gamma/\omega_r| \ll 1$ , it is possible to show for an electron plasma that [18]

$$\gamma = \frac{\pi}{2} \omega_{pe}^2 \left( \frac{\omega_r}{k} \right) \left. \frac{\partial f}{\partial v} \right|_{v=\omega_r/k}.$$

The physical explanation for the former relation follows from the fact that the interaction between a particle in the distribution and a wave propagating through the plasma will be fluctuating due to their relative velocities, and the net energy transfer will be negligible unless they have similar speeds. Then, the wave will only interact significantly with particles close to its phase velocity, accelerating those slightly slower, and slowing down those slightly faster. Therefore, if the slope of the distribution function at the phase velocity is positive (*i. e.* if there are more particles faster than slower at the vicinity of the wave speed), the wave will grow in amplitude taking kinetic energy from the distribution function, and if the slope of the distribution function is negative at the same speed, then the energy of the wave will decrease accelerating the particles, thus diminishing its amplitude.

### 2.2.2 Trapping and BGK modes

Consider a single finite-amplitude monochromatic wave with electrostatic potential

$$\Phi(x, t) = \Phi_0 \cos(kx - \omega_r t). \quad (2.13)$$

In the frame of reference of the wave,

$$\begin{aligned} x' &= x - \frac{\omega_r}{k}t, \\ v' &= v - \frac{\omega_r}{k}, \end{aligned}$$

the wave potential will be stationary,

$$\Phi'(x') = \Phi_0 \cos(kx'),$$

and the total energy of a single particle in this frame of reference will be

$$W'(x', v') = \frac{1}{2}mv'^2 + q\Phi_0 \cos(kx'), \quad (2.14)$$

where  $q$  and  $m$  are the charge and mass of the particle, respectively. Note that  $W'(x', v')$  is constant, and defines the trajectory of the particle in the phase space.

Fig. 2.3, shows trajectories with constant energy in the  $(x', v')$  phase space. It is possible to distinguish free-streaming regions,  $W' > 0$ , where the particles are passing with respect to the wave, and a region of trapping,  $W' < 0$ , where particles are condemned to bounce back-and-forth, traveling with the wave, trapped on its potential.

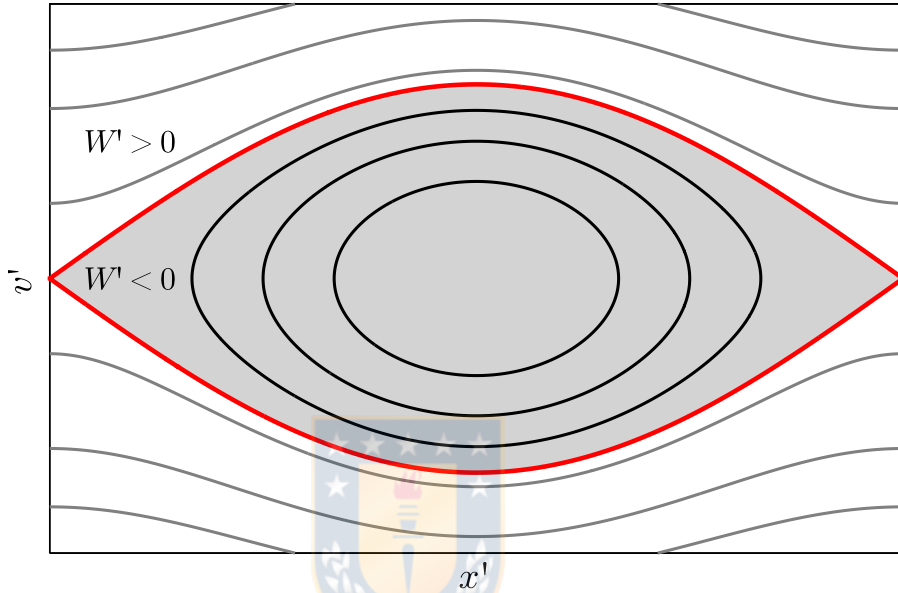


Figure 2.3: Constant contours of the single-particle energy,  $W'$ , in the frame of reference of the wave. The red contour marks the separatrix between the free-streaming ( $W' > 0$ , white background) and trapping ( $W' < 0$ , gray shade) regions.

Since the wave has finite amplitude, the wave-particle interactions are now expected to break the linear approximation taken before in this chapter, inducing finite modifications to the equilibrium distribution function. Similar to the linear case, the wave will interact with particles close to its phase velocity, accelerating the slower ones, and decelerating the faster ones. However, a big difference with the linear regime is that the wave-particle interactions that used to be restricted to an infinitesimal vicinity of the phase velocity, now are extended to what is shown in Fig. 2.3 as the trapping region, and the particles inside this region will be bouncing

with slightly different velocities each, until the density becomes mostly homogeneous (*i. e.* a *plateau* with  $\frac{\partial f}{\partial v} \sim 0$  is formed) and the wave amplitude reaches a constant value. This is illustrated on Fig. 2.4, where the evolution in time would be seen like the trapping region (gray shade) is spinning around the phase velocity of the wave (red line) until the plateau is formed.

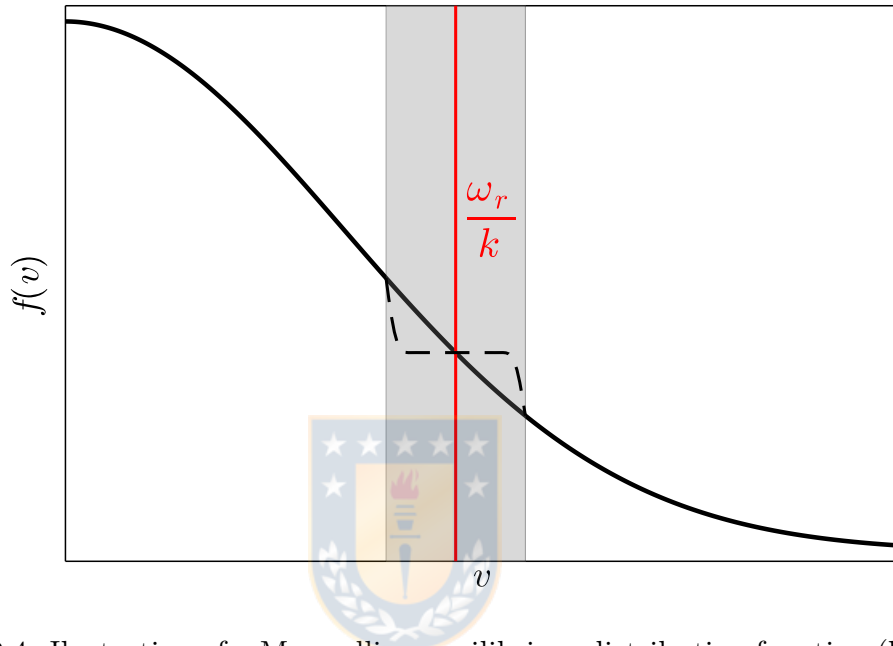


Figure 2.4: Illustration of a Maxwellian equilibrium distribution function (black solid line) and the formation of a *plateau* (black dashed line) due to nonlinear interaction with a wave  $(\omega_r, k)$ . The red vertical line marks the phase velocity of the wave and the gray shade marks the trapping region.

The asymptotic formation of the plateau in the velocity distribution function suggests the existence of nonlinear stationary solutions to the Vlasov-Poisson system of equations. This solutions were studied by Bernstein, Greene, and Kruskal [1], and hence they are called BGK modes. They considered the Vlasov-Poisson system of

equations in the frame of reference of the wave,

$$v' \frac{\partial f_j}{\partial x'} - \frac{q_j}{m_j} \frac{\partial \Phi'}{\partial x'} \frac{\partial f_j}{\partial v'} = 0, \quad (2.15)$$

$$\frac{\partial^2 \Phi'}{\partial x'^2} = -4\pi \sum_j q_j \int_{\mathbb{R}} f_j(x', v') dv', \quad (2.16)$$

and started constructing its exact solutions by posing the phase space distributions to depend only on the energy,  $W'$ , which trivially fulfills equation (2.15) since  $W'$  is a constant of motion. They found two ways to find the particular solutions from the Poisson equation, (2.16): (a) the *integral equation* method, also called the BGK method, consisting on prescribing the background equilibrium distribution and potential shape with little restrictions, and solving the integral equation returned from the Poisson equation to find the shape of the phase space distribution on the trapped region, and (b) the *differential equation* method, also called *Classical Potential*, Sagdeev or Schamel method, consisting on specifying the whole distribution function, integrating it to obtain the charge density, and solving the differential equation returned from the Poisson equation to find the potential. However, this method includes more subtleties.

In this manner, they found that an infinite family of solutions could be constructed to exactly fulfill the system of equations, without amplitude restriction, and with freedom to specify the shape of the potential (which does not even requires periodicity) or the shape of the trapped distribution function. For a more detailed review on the construction methods, refer to the excellent review on electron holes (a kind of solitary BGK-like mode) by Hutchinson [6].

It is important to mention that BGK modes are not a simple mathematical curiosity. They hold a very important role in plasma physics since they represent an ubiquitous family of waves, observed not only in countless simulations as the asymptotic result of linear instabilities [4] or perturbations leading to nonlinear Landau damping [5], but also in laboratory experiments [3], and satellite measurements [2].

Strictly speaking, the term BGK mode refers to a nonlinear, analytical solution

found to the Vlasov-Poisson system of equations. For this reason, the term BGK-like mode will be used to denote the nonlinear structures of the same nature arising from the plasma self-consistent dynamics, thus having a richer constitution.

### 2.2.3 Transverse instability of BGK modes

Although many kinds of BGK modes have been observed to be stable in 1–dimensional simulations, they often develop transverse sidebands leading to kinking and posterior break up of the mode when the particles are allowed to move transverse to the trapping direction.

Consider the ever-present soliton-like, traveling structures in space plasmas called electron holes (EH). They consist on regions of low electron density, causing a localized electric potential able to propagate self-consistently sustained by trapping of electrons. A more thorough introduction to EH is provided in the already mentioned review [6].

While EH are stable and able to propagate indefinitely on 1–dimensional simulations, unmagnetized PIC simulations have long shown that they break up on 2– or 3–dimensional simulations [7]. This effect has been called *transverse instability* of electron holes. It is controlled by the presence of a parallel magnetic field and high transverse velocity spread [19], and a theory for the mechanism of instability has just been proposed based on considerations of momentum conservation [20].

On the other hand, the kinetic transverse instability of periodic BGK modes is also under study. In the context of laser-plasma interaction, a theory for the transverse collapse of Large Amplitude Langmuir Waves has been developed under the name of filamentation instability [8], with qualitative agreement of PIC simulations [10], but cleaner Vlasov simulations suggest that the theory still requires improvements [11]. Similarly, numerical simulations in the same context have accounted for the transverse instability of Ion Acoustic Waves, but the transverse growth rates measured remain unexplained [12].



## 2.3 Vlasov-Poisson Simulations

The Vlasov-Poisson system of equations presents a number of attributes that render its solution a non-trivial problem. Some of these attributes are

- The system is *stiff*, meaning that explicit integration schemes will be unstable and fail to converge to the exact solution unless the integration step-size fulfills the Courant-Friedrichs-Levy (CFL) condition [21].
- The system exhibits nonlinear behavior inherited from the interaction between the distribution function with the electric field of the system, which is a function of the distribution function itself.
- The dynamics of the system depend not only on the configuration space, but also on the velocity space, implying that a  $d$ -dimensional plasma must be resolved considering a  $2d$ -dimensional phase space.
- While the system is conservative, it has the tendency to develop small-scale structures, resulting on artificial diffusion and loss of information if these scales are not resolved accordingly.

The last two properties imply that the Vlasov-Poisson equations are specially hard to solve in high-dimensional problems, since the number of points in phase space required to map the distribution function over a dense grid grows exponentially on the number of nodes considered per dimension, and also the computational resources required.

With the aforementioned difficulties in mind, several strategies have been designed to numerically solve the VP system, and they can be classified into either *particle* or *grid* methods.

Particle methods are the most classical approach to integrate the Vlasov-Poisson system of equations, and rely on the Lagrangian integration of the individual trajectories of a large number of particles along the characteristic curves of the Vlasov

equation. These methods yield reasonable results using relatively low numerical resources, but they suffer from statistical noise decreasing as  $n^{-1/2}$ , where  $n$  is the number of particles. On the other side, grid-based methods avoid the sampling noise inherent to particle methods through direct discretization of the phase space to an Eulerian grid. However, the stiffness and velocity-dependence of the system makes the discretization to simultaneously need a large number of points on each dimension, and a  $2d$ -dimensional phase space, which can render this kind of methods prohibitive with respect to the computational resources required, specially for  $d > 1$ .

To bypass the restrictions imposed by the stiffness of the system, an intermediate scheme denominated *backwards semi-Lagrangian*, was originally introduced in the context of weather prediction [22], and later incorporated to Vlasov simulations by Cheng and Knorr [23]. It consists on an Eulerian grid, where the distribution function at each grid point is computed by following the characteristic curves of the Vlasov equation starting from that point backwards in time, and mapping the distribution function on the resulting phase point to the grid. In this way, the integration of the distribution function resembles the integration of individual particles, thus avoiding the stability restrictions due to the stiffness of the system, but without incurring in the sampling errors which originate the statistical noise on particle methods. While this method still requires higher computational resources in comparison with particle methods, the increasing power of modern computing machines has turned them into a viable trade-off between performance and precision.

Another problem introduced by the regular discretization of the phase space is the appearance of *recurrence*. This complication consists in the fact that there is a minimum velocity length,  $\Delta v$ , that can be accessed by the simulation. This sets a cutoff in the Fourier conjugate for the velocity variable,  $\nu_{\max} = 2\pi/\Delta v$ , and therefore also sets a maximum period of time  $t_{\text{rec}} = \nu_{\max}/k = 2\pi/k\Delta v$  for which the information of a given wavenumber,  $k$ , can be resolved. After the so called recurrence time, the results will be repeated over and over just like a truncated Fourier series,

thus breaking the validity of the simulation. Nonetheless, multiple methods are used to suppress the effect of recurrence, such as adding a collisional or diffusive term on the right-hand-side of the Vlasov equation, although collisions are discouraged as a control for recurrence [24]. Other methods consist on adding a wavenumber cutoff at each time step [25], smoothing the velocity dependence of the distribution function by convolution against a continuous anisotropic filter at each time-step [23], or even solving an already filtered version of the Vlasov-Poisson system of equations [26].

Using the backwards semi-Lagrangian approach, spectral interpolation, and controlling recurrence by means of a continuous anisotropic filter, the author of the present work developed an open source library using the Julia programming language [13] which aims to provide an easy-to-use environment to numerically solve the Vlasov-Poisson system of equations on either 1 or 2 physical dimensions, together with tools to analyze the results in a generic way. The name of the library is “Vlasova.jl”. It has been tested against numerous test cases, including the two-dimensional and multi-species tests proposed by Barsamian *et al.* [27], and to the date of writing of this document it has a webpage<sup>2</sup> holding its documentation.

This section will explain in general terms how “Vlasova.jl” solves the Vlasov-Poisson system of equations. To this end the system will be nondimensionalized, and its solution will be shown to approximate to the solution of successive advection equations, each with analytical solution. Finally, a brief note will be presented on the existence of conserved quantities, and how they can be used to track the validity of the simulations performed.

---

<sup>2</sup><https://jgidi.gitlab.io/Vlasova.jl> (under development)

### 2.3.1 Dimensionless system of equations

The Vlasov equation for the species  $j$ , (2.1), together with equations (2.2)-(2.5) can be nondimensionalized using the dimensionless variables

$$t' = t\omega_{pe}, \quad (2.17a)$$

$$\mathbf{x}' = \mathbf{x}/\lambda_{De}, \quad (2.17b)$$

$$\mathbf{E}' = \frac{|q_e|}{m_e v_{te} \omega_{pe}} \mathbf{E}, \quad (2.17c)$$

$$\mathbf{v}'_j = \mathbf{v}/v_{tj}, \quad (2.17d)$$

$$f'_j = f_j/n_j v_{tj}^3, \quad (2.17e)$$

where  $m_e$  and  $q_e$  are the electron's mass and charge, respectively,  $\omega_{pe}$  is the electron plasma frequency,  $\lambda_{De}$  is the electronic Debye length.  $v_{tj}$  and  $n_j$  are the thermal speed the density of the species  $j$ . Proceeding in this manner, the dimensionless Vlasov-Poisson system of equations is obtained,

$$\frac{\partial f'_j}{\partial t'} + \nu_j \mathbf{v}'_j \cdot \frac{\partial f'_j}{\partial \mathbf{x}'} + \frac{\kappa_j}{\mu_j \nu_j} \mathbf{E}' \cdot \frac{\partial f'_j}{\partial \mathbf{v}'_j} = 0, \quad (2.18)$$

$$\frac{\partial}{\partial \mathbf{x}'} \cdot \mathbf{E}' = \sum_j \kappa_j \int_{\mathbb{R}^3} f'_j d^3 v'_j, \quad (2.19)$$

where

$$\nu_j = v_{tj}/v_{te}, \quad (2.20a)$$

$$\kappa_j = q_j/|q_e|, \quad (2.20b)$$

$$\mu_j = m_j/m_e. \quad (2.20c)$$

Until this point, primed quantities were used to refer to nondimensionalized variables, but since all quantities will be nondimensional from here on this chapter, all prime symbols will be dropped for convenience.

### 2.3.2 Symplectic interators

Symplectic integrators are numerical integration schemes designed to solve Hamiltonian systems, meaning that the conservation of the energy is implied in their construction. It is known that symplectic integrators keep the energy errors bounded in time [28], making them specially suitable for the long-time integration of conservative systems.

A class of the symplectic integrators is formed by the splitting methods [29], which will be reviewed now in the specific context of the Vlasov equation.

The dimensionless Vlasov equation, (2.18), can be rewritten

$$\frac{\partial f}{\partial t} = (L_j + N_j) f_j, \quad (2.21)$$

where  $L_j$  and  $N_j$  are differential operators given by

$$\begin{aligned} L_j &= -\nu_j \mathbf{v}_j \cdot \frac{\partial}{\partial \mathbf{x}}, \\ N_j &= -\frac{\kappa_j}{\mu_j \nu_j} \mathbf{E} \cdot \frac{\partial}{\partial \mathbf{v}_j}. \end{aligned}$$

On the one hand,  $L_j$  just depends upon  $\mathbf{x}$  and  $\mathbf{v}$ , and it is therefore a constant in time. On the other hand,  $N_j$  depends on the distribution function, but since the Vlasov equation defines the characteristic curves that make the distribution function constant,  $df/dt = 0$ , then  $N_j$  will also be constant along the same curves. That is,

$$\begin{aligned} \frac{d(L_j + N_j)}{dt} &= \frac{dN_j}{dt} \\ &= \frac{\partial N_j}{\partial f} \frac{df}{dt} \\ &= 0. \end{aligned}$$

Since  $(L_j + N_j)$  is a constant in time, then equation (2.21) can be directly integrated from time  $t$  to  $t + \Delta t$  to yield

$$f_j(\mathbf{x}, \mathbf{v}_j, t + \Delta t) = e^{\Delta t(L_j + N_j)} f_j(\mathbf{x}, \mathbf{v}_j, t). \quad (2.22)$$

Moreover, it is possible to use the Baker-Campbell-Hausdorff formula to factor out and approximate the propagator  $e^{\Delta t(L_j+N_j)}$  as a product of simpler operators, where the application of each one of them counts with analytical solution. Then, depending on the factorization chosen, different symplectic integration schemes will be generated.

### Second order integrator

Taking the second order approximation,

$$e^{\Delta t(L_j+N_j)} + O(\Delta t^3) = e^{\frac{\Delta t}{2}N_j} e^{\Delta t L_j} e^{\frac{\Delta t}{2}N_j},$$

one can express equation (2.22) as

$$f_j(\mathbf{x}, \mathbf{v}_j, t + \Delta t) \approx e^{\frac{\Delta t}{2}N_j} e^{\Delta t L_j} e^{\frac{\Delta t}{2}N_j} f_j(\mathbf{x}, \mathbf{v}_j, t), \quad (2.23)$$

where the application of the propagator  $e^{aL_j}$  over the distribution function  $f_j$ , with  $a$  a constant scalar, is the trivial solution to the advection equation,

$$\frac{\partial f_j}{\partial t} - L_j f_j = 0,$$

when integrated over a time interval  $a$ , and the same reasoning holds for the propagator  $e^{aN_j}$ . In this manner, equation (2.23) provides an algorithm to approximate  $f_j(\mathbf{x}, \mathbf{v}, t + \Delta t)$  through the integration during the half of a time step,  $\Delta t/2$ , of a velocity advection equation,

$$\frac{\partial f_j}{\partial t} + \frac{\kappa_j}{\mu_j \nu_j} \mathbf{E} \cdot \frac{\partial f_j}{\partial \mathbf{v}_j} = 0, \quad (2.24)$$

then integrating for a whole time step,  $\Delta t$ , a position advection equation,

$$\frac{\partial f_j}{\partial t} + \nu_j \mathbf{v}_j \cdot \frac{\partial f_j}{\partial \mathbf{x}} = 0, \quad (2.25)$$

and finally integrating the velocity advection equation, (2.24), for another half of a time step,  $\Delta t/2$ . Note that this corresponds to the well known velocity-Verlet integration scheme [30].

This integration scheme is notable not only because of its simplicity, but also because it was the first splitting method proposed to solve the Vlasov-Poisson system of equations in the outstanding article by Cheng and Knorr [23], and today continues to be the most widely used scheme to integrate conservative systems, including the Vlasov equation.

### Higher-order integrators

It is possible to construct higher-order approximations [31], but negative time-steps may appear. This is undesirable since moving back-and-forth in time introduces higher numerical errors and artificially increments entropy.

However, it is possible to avoid the integration of negative time-steps by retaining the commutator

$$[N_j, [L_j, N_j]] = -\frac{\kappa_j^2}{\mu_j^2 \nu_j} \frac{\partial |\mathbf{E}|^2}{\partial \mathbf{x}} \cdot \frac{\partial}{\partial \mathbf{v}_j}$$

in the expansion of the exponential propagator from equation (2.22).

Furthermore, since the differential operator just shown commutes with  $N_j$ ,

$$[N_j, [N_j, [L_j, N_j]]] = 0,$$

then it can be incorporated as a simple correction to the forcing term while integrating a neighboring velocity advection equation.

Integrators built with this method are usually said to have force gradient corrections, and a good example of one of them is the fourth-order integrator A from Chin [32], consisting on the resolution of 5 advection equations: First, a velocity advection for a sixth of a time-step  $\Delta t/6$ . Then, a position advection for half a time-step,  $\Delta t/2$ . Later, a velocity advection with a gradient correction to the forcing term,  $\mathbf{E}' = \mathbf{E} + \frac{(\Delta t)^2}{48} \frac{\kappa_j}{\mu_j} \frac{\partial |\mathbf{E}|^2}{\partial \mathbf{x}}$ , for two thirds of a time-step,  $2\Delta t/3$ . Then a position advection for half a time-step,  $\Delta t/2$  and finally a velocity advection for another sixth of a time-step,  $\Delta t/6$ .

### 2.3.3 Solution of the advection equations

As shown in the previous section, there are splitting methods allowing to approximate the solution to the Vlasov equation as the solution of a combined sequence of the two advection equations

$$\frac{\partial f_j}{\partial t} + \nu_j \mathbf{v}_j \cdot \frac{\partial f_j}{\partial \mathbf{x}} = 0, \quad (2.26a)$$

$$\frac{\partial f_j}{\partial t} + \frac{\kappa_j}{\mu_j \nu_j} \mathbf{E} \cdot \frac{\partial f_j}{\partial \mathbf{v}_j} = 0, \quad (2.26b)$$

which can be readily solved by means of Fourier transforms.

Defining the Fourier transform,

$$\begin{aligned} \widehat{g}(k) &= \mathcal{F}\{g\}(k), \\ &= \int_{\mathbb{R}} e^{-ikx} g(x) dx, \end{aligned}$$

and its inverse,

$$\begin{aligned} g(x) &= \mathcal{F}^{-1}\{\widehat{g}\}(x), \\ &= \frac{1}{2\pi} \int_{\mathbb{R}} e^{ikx} \widehat{g}(k) dk, \end{aligned}$$

one can transform equation (2.26a) in the space variable,  $\mathbf{x} \rightarrow \mathbf{k}$ , to yield

$$\frac{\partial \widehat{f}_j(\mathbf{k}, \mathbf{v}_j, t)}{\partial t} - i\nu_j \mathbf{k} \cdot \mathbf{v}_j \widehat{f}_j(\mathbf{k}, \mathbf{v}_j, t) = 0,$$

which integrated from time  $t$  to  $t + \Delta t$  returns

$$\widehat{f}_j(\mathbf{k}, \mathbf{v}_j, t + \Delta t) = \exp(i\Delta t \nu_j \mathbf{k} \cdot \mathbf{v}_j) \widehat{f}_j(\mathbf{k}, \mathbf{v}_j, t).$$

Note that in the Fourier space, the exponential term acts as a change of phase. In fact, taking the inverse Fourier transform on the last equation reads

$$f_j(\mathbf{x}, \mathbf{v}_j, t + \Delta t) = f_j(\mathbf{x} + \Delta t \nu_j \mathbf{v}_j, \mathbf{v}_j, t), \quad (2.27)$$

providing the analytical solution to the position advection equation (2.26a), when integrated for a time step  $\Delta t$ .



Similarly, equation (2.26b) can be integrated from time  $t$  to  $t + \Delta t$  on the Fourier space for the velocity variable,  $\mathbf{v}_j \rightarrow \mathbf{p}$ , to yield

$$\widehat{f}_j(\mathbf{x}, \mathbf{p}, t + \Delta t) = \exp\left(i\Delta t \frac{\kappa_j}{\mu_j \nu_j} \mathbf{E} \cdot \mathbf{p}\right) \widehat{f}_j(\mathbf{x}, \mathbf{p}, t),$$

which back in the real space reads

$$f_j(\mathbf{x}, \mathbf{v}_j, t + \Delta t) = f_j\left(\mathbf{x}, \mathbf{v}_j + \Delta t \frac{\kappa_j}{\mu_j \nu_j} \mathbf{E}, t\right). \quad (2.28)$$

Consequently, the advection equations may be solved using the interpolation method of preference, be it spectral, Galerkin, polynomial, or whichever results adequate to a particular situation. It must be noted that, in order for the expansion of the operator in (2.22) to make sense, each velocity advection on a sequence must be performed having recalculated the forcing term,  $\mathbf{E}$ , from the updated distribution function.

### 2.3.4 Electrostatic force calculation

From the dimensionless Gauss equation (2.19), and using the definition of Fourier transform (A.4a) and its inverse (A.4b), it is straightforward to show that the forcing term in the Vlasov equation can be obtained as

$$\mathbf{E}(\mathbf{x}, t) = \mathcal{F}^{-1} \left\{ i \frac{\mathbf{k}}{|\mathbf{k}|^2} \mathcal{F} \{ \rho \} \right\}, \quad (2.29)$$

where

$$\rho(\mathbf{x}, t) = \sum_j \kappa_j \int_{\mathbb{R}} f_j d^3 v_j$$

is the charge density collected from all the species in the plasma,  $\mathcal{F}$  is the Fourier transform on the space variable, and  $\mathcal{F}^{-1}$  its inverse.

Since the electric field depends on space but not on velocity, it is conserved across velocity advectons, but must be recalculated after position advectons.

### 2.3.5 Validity of the simulations

The Vlasov equation can be implicitly written as


$$\frac{df}{dt} = 0,$$

implying that any well behaved function depending only on the distribution function,  $C(f)$ , must be conserved in time as well. Therefore, the ability of a Vlasov simulation to resolve the system properly can be verified through the conservation of quantities of this kind.

Many important conserved quantities may be constructed, but the ones most widely verified are the total energy,

$$E_{tot} = \frac{1}{2} \int_{\mathbb{R}^3} \int_{\mathbb{R}^3} |\mathbf{v}|^2 f d^3x d^3v + \frac{1}{2} \int_{\mathbb{R}^3} |\mathbf{E}|^2 d^3x, \quad (2.30)$$

the number of particles,


$$N = \int_{\mathbb{R}^3} \int_{\mathbb{R}^3} f d^3x d^3v, \quad (2.31)$$

and the entropy,

$$S = \int_{\mathbb{R}^3} \int_{\mathbb{R}^3} f \log f d^3x d^3v. \quad (2.32)$$

# Chapter 3

## Results and Discussion

### 3.1 Numerical setup

To analyze the transverse instability of self-consistently formed BGK-like modes, direct simulations of the Vlasov-Poisson system of equations, (2.1)-(2.5), are performed for 2-dimensional plasmas using the methods presented in section 2.3: Vlasov-Poisson Simulations.

The equilibrium distribution functions considered are uniform in space given by

$$f(x, y, v_x, v_y) = n_e f_{\parallel}(v_x) f_{\perp}(v_y), \quad (3.1)$$

where  $n_e$  is the electron density.

On the direction of  $y$ , the velocity distributions are Maxwellian,

$$f_{\perp}(v) = \frac{1}{\sqrt{2\pi}v_{te}} \exp\left[-\frac{v^2}{2v_{te}^2}\right], \quad (3.2)$$

where  $v_{te} = \sqrt{k_B T_e / m_e}$ ,  $T_e$  and  $m_e$  are the thermal speed, temperature and mass of the electrons, respectively, and  $k_B$  is the Boltzmann's constant.

Linearly unstable bump-on-tail distributions are used along the direction of  $x$ ,

$$f_{\parallel}(v) = (1 - \varepsilon) f_c(v - V_c) + \varepsilon f_b(v - V_b), \quad (3.3)$$

where

$$f_j(v) = \frac{1}{\sqrt{2\pi}v_{tj}} \exp\left[-\frac{v^2}{2v_{tj}^2}\right], \quad (3.4)$$

taking the index  $j$  may refer to the core ( $j = c$ ) or the beam ( $j = b$ ). The thermal speed of the core and the beam are  $v_{tc} = v_{te}$  and  $v_{tb} = 0.5v_{te}$ , respectively, and  $\varepsilon$  controls the density of the beam. Cases with  $\varepsilon = 0.05$ ,  $\varepsilon = 0.1$  and  $\varepsilon = 0.2$  are studied.

For each value of the beam density,  $\varepsilon$ , the minimum drift velocity for the distribution to be unstable,  $V_{th}$ , is calculated from equation 2.10. The threshold values are  $V_{th}^{\varepsilon=0.05} = 2.82v_{te}$ ,  $V_{th}^{\varepsilon=0.1} = 1.97v_{te}$ , and  $V_{th}^{\varepsilon=0.2} = 2.42v_{te}$ . Then, a group of simulations are run with different relative velocities between the beam and the core,  $V_d = V_b - V_c$ , within the range  $V_{th} \leq V_d \leq 5.5v_{te}$ . To avoid breaking the electrostatic approximation, the individual velocities of the core and the beam are fixed such that the frame of reference of the simulation is on the center of mass,  $(1 - \varepsilon)V_c + \varepsilon V_b = 0$ .

For the configurations mentioned, the dispersion relation (2.10) was scanned to find the complex frequencies,  $\omega = \omega(\mathbf{k})$ , allowed according to the linear theory for each wavevector,  $\mathbf{k}$ , fitting in the simulational box, and the most unstable configuration always lied parallel to the beams. Fig. 3.1 shows contour lines of the maximum growth rate found for each wavevector,  $\mathbf{k} = (k_x, k_y)$ , considering a beam density of 10% ( $\varepsilon = 0.1$ ) and a drift velocity  $V_d/v_{te} = 3$ .

To emulate thermal noise, all distributions are initialized with a very low-amplitude ( $\sim 10^{-15}$ ) uniform distribution of random density perturbations in space, allowing the excitation of all the modes fitting in the phase space box. Additionally, to precipitate the formation of a BGK-like mode from the most excited mode of the simulation, a greater density perturbation is added,

$$\delta n(\mathbf{x}) = 10^{-8} \cos(\mathbf{k}_0 \cdot \mathbf{x}), \quad (3.5)$$

where  $\mathbf{k}_0 = k_0 \hat{\mathbf{x}}$  is the most unstable mode predicted by the linear dispersion relation. This is performed in order to ensure that oblique modes still have small amplitude

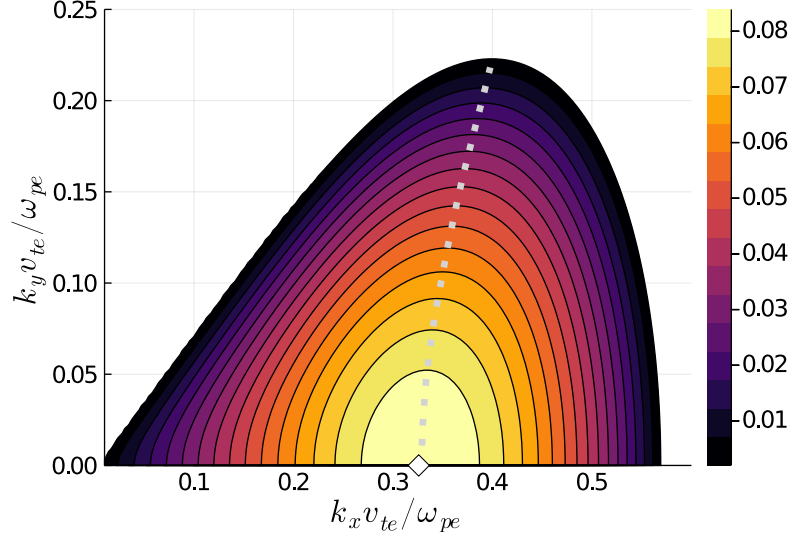


Figure 3.1: Maximum growth rates scanned from the linear dispersion relation (2.10), as a function of the wavevector,  $\mathbf{k} = (k_x, k_y)$ , for a beam with density of 10% ( $\varepsilon = 0.1$ ) and a drift  $V_d/v_{te} = 3$ . The white diamond marks the most unstable configuration and the gray dashed line follows the highest growth rate for each value of  $k_y$ . Only growth rates,  $\gamma/\omega_{pe} > 10^{-3}$  are shown.

when the nonlinear structure parallel to the beam has formed, consequently allowing the study of the transverse instability around the BGK-like state.

The phase space lengths were chosen  $L_x = 2\pi/k_0$  along  $x$ , to rule out the sideband instability [33, 34], and  $L_y = 400\pi\lambda_{De}$  along  $y$ , to allow the development of long wavelengths (small wavenumbers) that are characteristic of the transverse instability of BGK-like modes [11]. The velocity dimensions are resolved within the intervals  $v_x/v_{te} \in [-6, 12]$  and  $v_y/v_{te} \in [-6, 6]$ , respectively.

The discretization resolutions consisted of a time-step of  $dt\omega_{pe} = 0.1$ ,  $N_x = 128$  nodes in the space dimension  $x$ ,  $N_y = 64$  nodes along in the space dimension  $y$ ,  $N_{v_x} = 1024$  nodes in the velocity dimension  $v_x$ , and  $N_{v_y} = 64$  nodes along the velocity dimension  $v_y$ , where  $x$  and  $v_x$  are parallel to the beam, and  $y$  and  $v_y$  are perpendicular to the beam.

To suppress the effect of recurrence, every velocity advection incorporates anti-aliasing of the distribution function by convolution against a filter function with shape

$$\widehat{G}(\nu) = \exp \left[ -36 \left( \frac{\nu}{\nu_{\max}} \right)^{36} \right]$$

on the Fourier space, where  $\nu$  is the conjugate variable of the velocity component to filter, and  $\nu_{\max}$  is the maximum value of  $\nu$ .

The symplectic velocity-Verlet integrator was used in time. There was no need to use a higher-order integrator since the biggest error source lies on space rather than time discretization, whereas energy conservation was always accomplished up to a relative order of  $10^{-5}$ , and convergence tests showed no change on behavior when scaling up the number of phase space nodes.

## 3.2 Results

### 3.2.1 Description of the instability

To introduce the general behavior of the 2–dimensional simulations in contrast to the better known 1–dimensional bump-on-tail evolution, Fig. 3.2 displays the electrostatic evolution of a linearly unstable bump-on-tail configuration with  $\varepsilon = 0.1$  and  $V_d/v_{te} = 3.0$  when: (a) the dynamics of the plasma are restricted along a single dimension parallel to the beam, or (b) allowed to develop in the dimension perpendicular to the beam as well. In 1 dimension, the plasma passes mainly through two well-known stages: Stage I, characterized by the exponential growth of the initial perturbation, but before it gets large enough for nonlinear effects come into play, and stage II, after the energy of the excited mode saturates and reaches a stable and quasi-steady BGK-like state.

When the plasma has a dimension transverse to the bump-on-tail configuration, the evolution of the system is different from the 1–dimensional case and 4 stages are

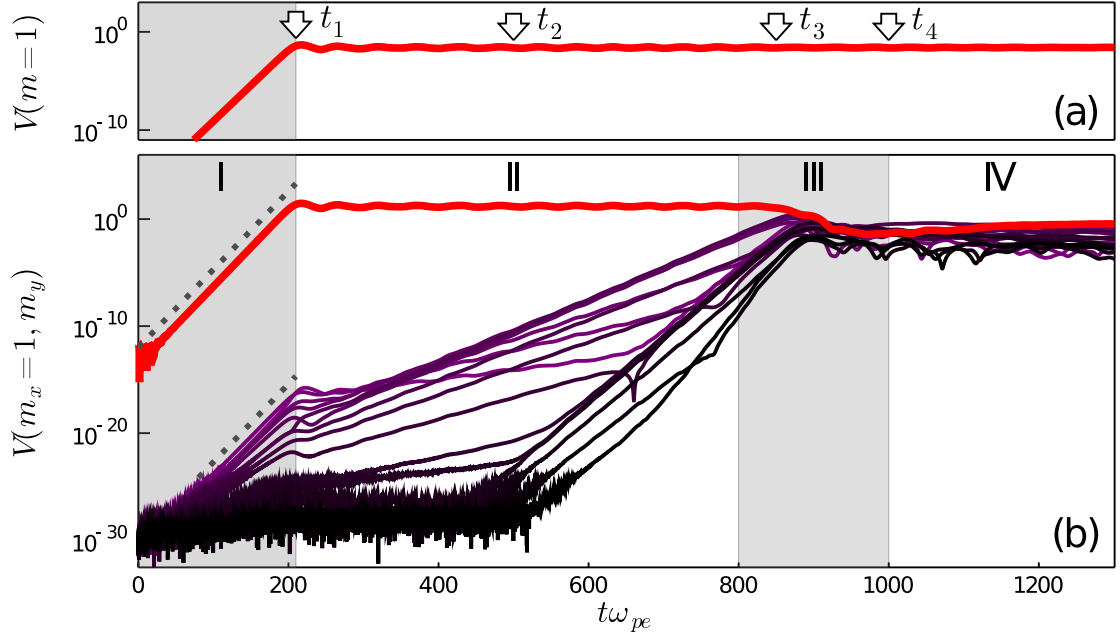


Figure 3.2: Spectral decomposition of the electrostatic energy. On the bottom panel, (b), the energy of the perturbed mode,  $(k_0, 0)$  (in red), and its first 15 transverse harmonics,  $(k_0, k_y)$  (from purple to black, as  $k_y$  gets larger), on a 2-dimensional simulation with  $\varepsilon = 0.1$  and  $V_d/v_{te} = 3$ . Gray dotted lines stand for the growth rates predicted from the linear dispersion relation (2.10). On top, (a), the energy of the perturbed mode,  $k = k_0$  on an equivalent simulation restricted to 1-dimensional evolution. White arrows mark the instants shown on the phase-space panels of Fig. 3.3. On both panels a logarithmic scale is used for the vertical axis, and gray/white backgrounds mark different stages during the evolution of the systems.

recognized. During stage I, additional to the exponential growth of the mode parallel to the beam, there is also exponential growth of waves oblique to the beam, which origin from the noise level and present growth rates coincident with the predictions from linear theory. The growth rates expected according to the linear dispersion relation, (2.10), are shown in Figure 3.1.

When the amplitude of the parallel mode is large enough for nonlinear effects to

come into play, it saturates transitioning to stage II, and the growth of oblique modes is temporarily arrested. After this short transition, oblique modes start growing again, although with growth rates smaller than in stage I and the most excited modes during stage I do not necessarily match the most excited modes in stage II. Moreover, the amplitudes of the oblique modes inherit oscillations from the amplitude of the already-saturated mode.

Oblique wavevectors continue to grow in time until their amplitude is comparable to the amplitude of the wave parallel to the beam. When this happens, at stage III, the previously saturated mode collapses, losing a few orders of magnitude in energy due to this purely multi-dimensional effect.

After the collapse of the wave parallel to the beam, at stage IV, the state of the plasma is characterized by the nonlinear superposition of a multitude of transverse harmonics of the wave originally excited. Long runs have been performed, and this state seems to last indefinitely.

Figure 3.3 displays the formation and evolution of a very similar phase-space vortex on both simulations, with either 1 physical dimension (a), (b), (c) and (d), or 2 physical dimensions, (e), (f), (g) and (h). The same instants are shown for both simulations, and correspond to the white arrows in Fig. 3.2(a). In 1 dimension, the structure formed remains stable and homogenizes as time goes on. However, in 2 dimensions, the vortex eventually starts to lose coherence (g) and finally collapses. Notice from panels (b) and (f) that the evolution of the averaged phase space in 2 dimensions looks identical to the evolution in 1 dimension before the transverse harmonics are large enough to disturb the vortex.

Figure 3.4 shows the velocity profile of the electron distribution function at three instants: (a) and (d) at the start of the simulation  $t\omega_{pe} = 0$ , (b) and (e) after the BGK-like structure parallel to the beam is formed but before it starts losing coherence  $t\omega_{pe} = 700$ , and (c) and (f) after the transverse collapse, deep into the stage IV  $t\omega_{pe} = 1500$ .



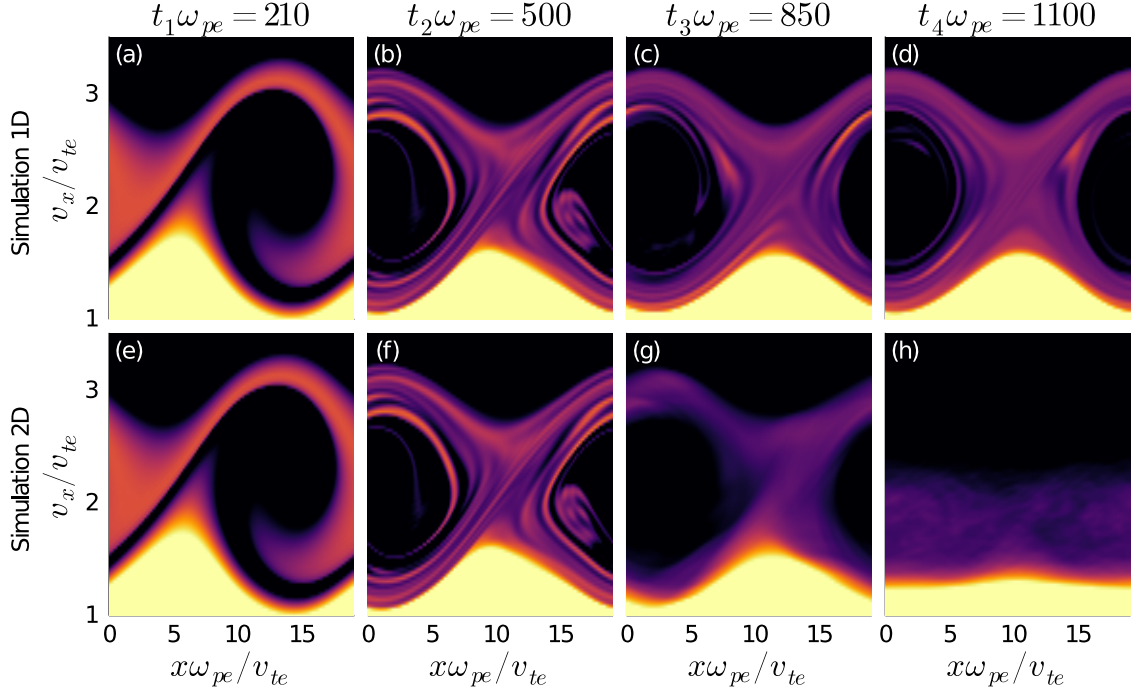


Figure 3.3: Phase-space vortex formed in 1– and 2–dimensional simulations with  $\varepsilon = 0.1$  and  $V_d/v_{te} = 3$ . The four panels on top, (a) to (d), correspond to the electron distribution function on a 1–dimensional simulation, and the four panels on the bottom, (e) to (h), to the transverse-averaged electron distribution function,  $\langle f_e \rangle(x, v_x)$ , on a 2–dimensional simulation. Times  $t_1$  to  $t_4$  correspond to the white arrows on Fig. 3.2. Yellow/black color stands for a higher/lower density of electrons. The colorscale is logarithmic, and its limits have been restricted to show only levels relevant to the vortex.

After the parallel BGK-like mode saturates, (b) and (e), the height of the beam is decreased and the well known *plateau* is formed between the core and the beam at the phase velocity of the BGK-like mode,  $v_\phi/v_{te} \approx 2.1$ , reducing the steepness of the beam. The three velocity cuts (b) show a distribution similar to the BGK-like steady equilibrium classical from 1–dimensional bump-on-tail simulations. For times posterior to the collapse, (c) and (f), the cut for  $v_y = 0$  (blue) shows the *plateau* to be further flattened around  $v_x = v_\phi$  while cuts with  $v_{te} \neq 0$  (red and green) show the

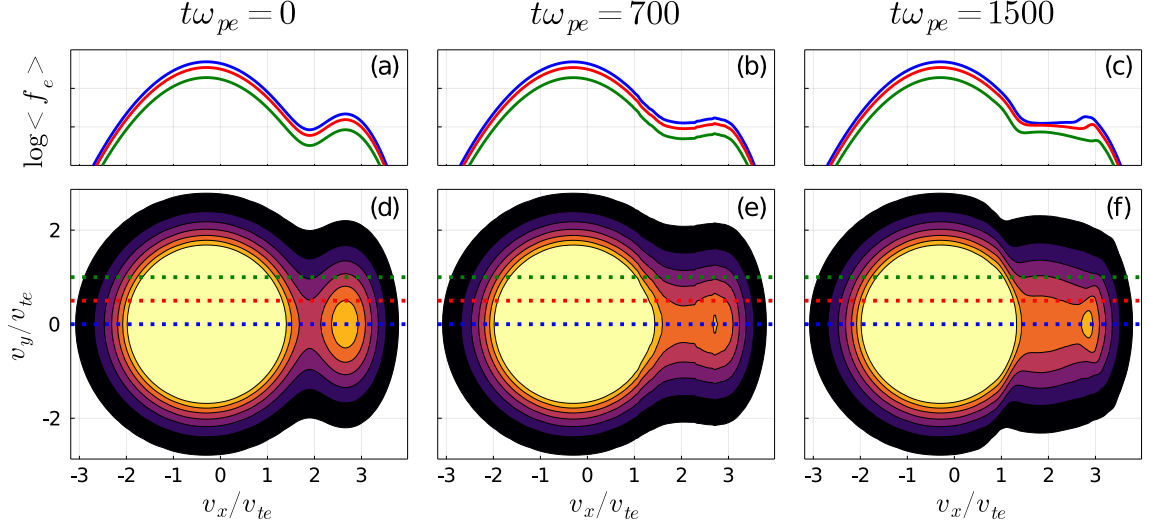


Figure 3.4: Velocity profile of the averaged electron distribution function,  $\langle f_e \rangle(v_x, v_y)$  on a simulation with  $\varepsilon = 0.1$  and  $V_d/v_{te} = 3$ . The bottom panels (d), (e) and (f) show contour lines of the distribution, and the top panels (a), (b) and (c), cuts of for  $v_y/v_{te} = 0$  (blue),  $v_y/v_{te} = 0.5$  (red) and  $v_y/v_{te} = 1$  (green). Three instants are shown: (a) and (d) at the start of the simulation  $t\omega_{pe} = 0$  on stage I; (b) and (e) when the BGK-like mode parallel to the beam dominates on stage II  $t\omega_{pe} = 700$ ; and (c) and (f) after the transverse collapse on stage IV  $t\omega_{pe} = 1500$ . The dashed colored lines in the bottom panels mark the velocity cuts shown with the same colors in the panels above.

formation of local maxima for  $v_x \sim v_\phi$ , evolving towards flattening and formation of a *plateau* also in the direction transverse to the beam. The similarity of this picture with the formation of the parallel BGK-like mode from the bump-on-tail equilibrium suggests the possibility of explaining the transverse instability as the consequence of a linearly unstable equilibrium velocity distribution, which could be studied through linearization of the Vlasov-Poisson system of equations around a model of the BGK equilibrium. However, such a model would not only depend on velocity, but also on space, as a density depletion is required for trapping to take place.

Figure 3.5 displays the power spectrum of the averaged charge density in a simu-

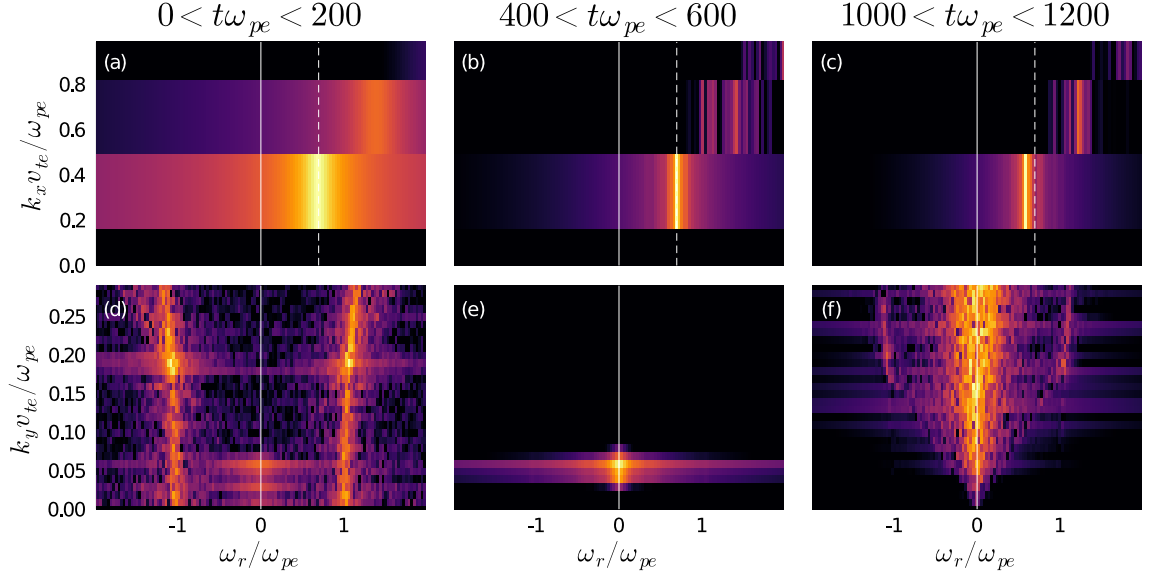


Figure 3.5: Power spectrum of the averaged electron charge density for a 2-dimensional simulation with  $\varepsilon = 0.1$  and  $V_d/v_{te} = 3$ . Upper panels (a), (b), and (c), show the power spectrum parallel to the beam,  $(\omega, k_x)$ . Bottom panels, (d), (e), and (f), the power spectrum transverse to the beam,  $(\omega, k_y)$ . Three time ranges are shown: (a) and (d) during stage I, (b) and (e) during stage II, and (c) and (f) during stage IV. The solid vertical lines mark  $\omega_r = 0$  and the dashed vertical lines mark  $\omega_0/\omega_{pe} = 0.695$ , the frequency predicted from linear theory for the mode initially excited  $(k_x, k_y) = (k_0, 0)$ . The colorscale is logarithmic and it has been normalized against the maximum power for each case, which is: (a)  $8 \cdot 10^7$ , (b)  $3 \cdot 10^{10}$ , (c)  $3 \cdot 10^8$ , (d)  $5 \cdot 10^{-18}$ , (e)  $2 \cdot 10^{-7}$ , and (f)  $2 \cdot 10^2$ .

lation with  $\varepsilon = 0.1$  and  $V_d/v_{te} = 3$ . Panels on top (a), (b) and (c) display the power distribution on the frequency and parallel wavenumber,  $(\omega, k_x)$ , while the bottom panels (d), (e) and (f) display the power distribution on the frequency and transverse wavenumber,  $(\omega, k_y)$ . Three temporal ranges are shown: (a) and (d) on stage I for  $0 < t\omega_{pe} < 200$ , (b) and (e) on stage II for  $400 < t\omega_{pe} < 600$ , and (c) and (f) on stage IV for  $1000 < t\omega_{pe} < 1200$ . Notice that the big step-size in  $k_x$  is due to

the fact that the space length along  $x$  was chosen  $L_x = 2\pi/k_0$  to rule out sideband instabilities, yielding a spectral resolution along this direction of  $\Delta k_x = k_0$ .

From panel (a), the stage I of the simulation is dominated by the initially excited mode parallel to the beam, with frequency correctly predicted from equation (2.10), corresponding to a pseudo-acoustic branch. For the same time range, on the direction transverse to the beam (d) one can observe the presence of Langmuir waves excited from the initial noise distribution, which are mostly undamped.

On stage II, panel (b) shows that the mode initially excited still dominates, consistent with Fig.3.2(b), and panel (e) shows the appearance of transverse waves with  $k_y \neq 0$  and  $\omega = 0$ , accounting for the presence of particles resonating with  $v_y = 0$ .

After the collapse on stage IV, the maximum power on panel (c) is considerably smaller in comparison to panel (b) (details on the caption of the figure), and the dominating mode has suffered a negative frequency shift. In the transverse direction (f) almost the entirety of transverse wavenumbers,  $k_y$ , are excited around  $\omega_r = 0$ . That is, a nonlinear superposition of non-propagating modes of all lengths in the transverse direction fill the phase-space. The appearance of symmetric Langmuir waves with  $k_y v_{te}/\omega_{pe} > 0.15$  is also observed.

### 3.2.2 Analysis of the transverse growth rates

Figure 3.6 shows the growth rate of the oblique modes  $(k_0, k_y)$  during the first part of stage II as a function of the transverse wavenumber,  $k_y$ , measured from a group of simulations with beam density  $\varepsilon = 0.1$  and a range of relative drift velocities. Lines with different color represent simulations with different drift velocity. White diamonds mark the most unstable transverse wavenumber measured at each simulation and the red line is a quadratic fit of the maximum growth rate,  $\gamma_m$ , as a function of the transverse wavenumber,  $\gamma_m(k_y) = 0.392k_y + 4.938k_y^2$ . The fit is adjusted for drift velocities  $V_d/v_{te} \leq 4.5$ .

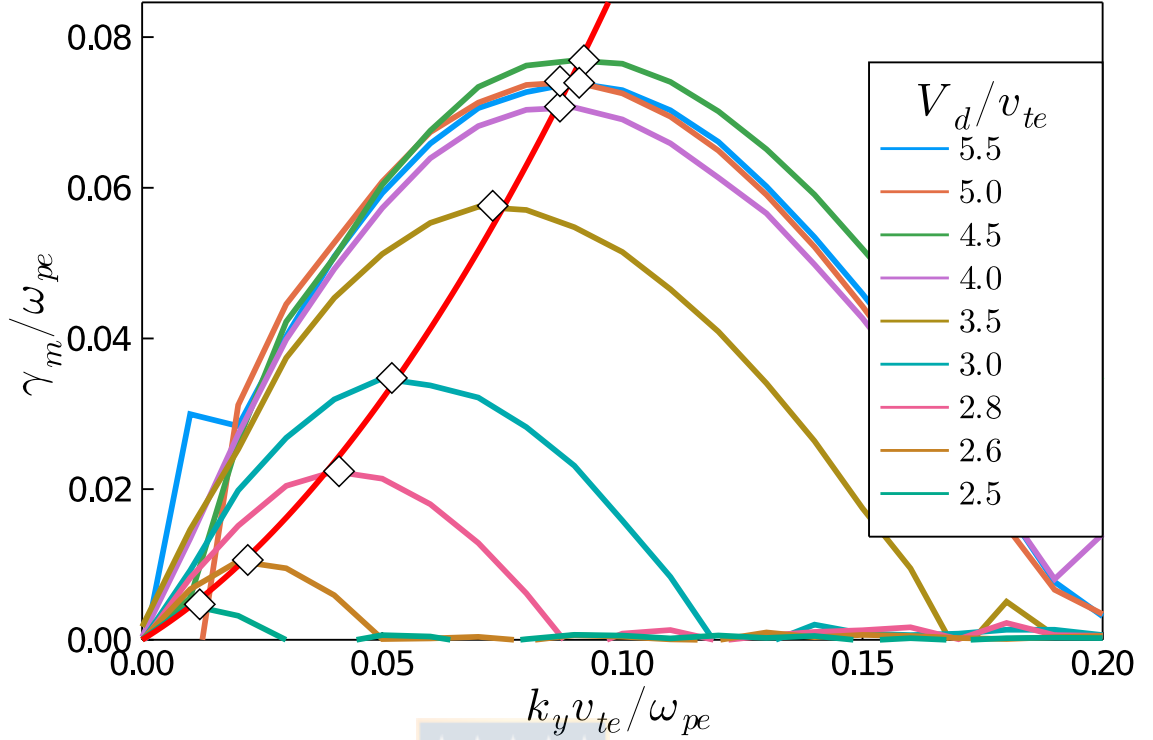


Figure 3.6: Transverse growth rates as a function of the transverse wavenumber,  $k_y$ . Beam density  $\varepsilon = 0.1$ . Lines of different colors are simulations with different initial drift velocity,  $V_d$ . White diamonds mark the maximum transverse growth rate,  $\gamma_m$ , and the red line is a quadratic fit for  $V_d/v_{te} \leq 4.5$ ,  $\gamma_m(k_y) = 0.392k_y + 4.938k_y^2$ .

The growth rates of the transverse wavenumbers has the shape of a symmetric bell. The range of excited wavenumbers (the bell width) and the maximum growth rate (the bell height) are growing functions of the initial drift velocity in the range  $v_{th}^{\varepsilon=0.1} < V_d < 4.5v_{te}$ , and saturate for  $V_d/v_{te} > 4.5$ . In all of the simulations shown, the bell starts growing approximately with  $\gamma_m = 0$  for  $k_y = 0$ , with deviations for  $V_d/v_{te} > 4.5$ , which are harder to measure since the amplitude of the parallel BGK-like mode formed oscillates violently, and its modulation is inherited to the oblique modes.

During stage I, the growth rates are higher for wavevectors aligned with the

beam,  $k_y = 0$ . In stage II, however, the maximum growth rate,  $\gamma_m$ , is achieved for transverse wavenumbers  $k_y \neq 0$ , which implies the existence of a minimum angle with respect to the beam for which the oblique modes are excited by the transverse instability with its greater effect.

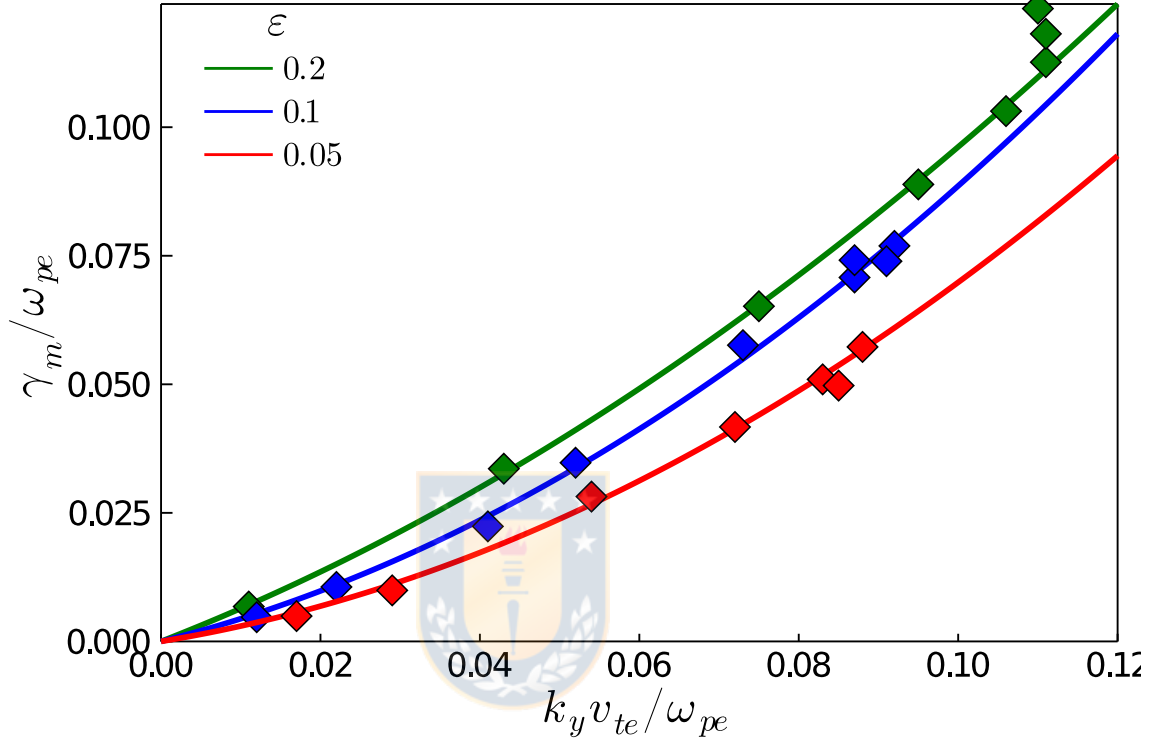


Figure 3.7: Maximum transverse growth rate,  $\gamma_m$ , as a function of the transverse wavenumber,  $k_y$ . Each diamond is an individual simulation. Colors red, blue and green stand for  $\epsilon = 0.05$ ,  $\epsilon = 0.1$  and  $\epsilon = 0.2$ , respectively. Solid lines are quadratic fits for  $V_d/v_{te} \leq 4.5$  for each group of simulations: in red  $\gamma_m^{\epsilon=0.05}(k_y) = 0.254k_y + 4.439k_y^2$ , in blue  $\gamma_m^{\epsilon=0.1}(k_y) = 0.392k_y + 4.9384k_y^2$ , and in green  $\gamma_m^{\epsilon=0.2}(k_y) = 0.605k_y + 3.564k_y^2$ .

Figure 3.7 displays the maximum growth rate as a function of the transverse wavenumber for three groups of simulations: in red with beam density  $\epsilon = 0.05$ , in blue with  $\epsilon = 0.1$ , and in green  $\epsilon = 0.2$ . The solid lines are quadratic fits for each

group, adjusted to the data with  $V_d/v_{te} < 4.5$ .

The maximum transverse growth rates from the groups of simulations with  $\varepsilon = 0.05$  and  $\varepsilon = 0.2$  also follow an approximately quadratic dependence on the transverse wavenumber, until a saturation value for the maximum wavenumber is reached, which happened in the three groups approximately at  $V_d/v_{te} = 4.5$ . However, for  $\varepsilon = 0.05$  (red) and  $\varepsilon = 0.1$  (blue), the maximum growth rates saturated approximately at the same drift velocity as the transverse wavenumbers, forming clumps on Fig. 3.7, while only the transverse wavenumbers saturated for  $\varepsilon = 0.2$  (green), and the maximum growth rates continued incrementing for higher drift velocities.

Figure 3.8 shows the maximum transverse growth rates measured on the first part of stage II (diamonds), and the growth rates of the same modes during stage I calculated from equation (2.10) (circles), for the groups of simulations with  $\varepsilon = 0.05$  (red),  $\varepsilon = 0.1$  (blue) and  $\varepsilon = 0.2$  (green). Solid lines are quadratic fits of the measured maximum growth rates and the dashed lines are quadratic fits for the linear growth rates. White stars mark the drift velocity threshold for the bump-on-tail with each beam density to be unstable.

One can observe from Fig. 3.8 that the maximum transverse growth rates on stage II approach to zero at the same instability thresholds as the growth rates from the initial bump-on-tail distribution on stage I, suggesting that the transverse instability around the BGK-like mode and the initial bump-on-tail instability have a common nature. Furthermore, whenever the bump-on-tail instability is present, the transverse instability will also appear and they will be strongly correlated.

Figure 3.9 relates the maximum transverse growth rate,  $\gamma_m$ , with the growth rate of the most unstable beam-mode during stage I,  $\gamma_L$ , obtained from linear theory. For the three groups of simulations, the growth rates of the transverse instability around the BGK-like mode, and the growth rate during stage I of the wave which evolved into the BGK-like mode follow an approximately linear relation. Moreover, the growth rates of both instabilities are related through a simple multiplicative factor, which

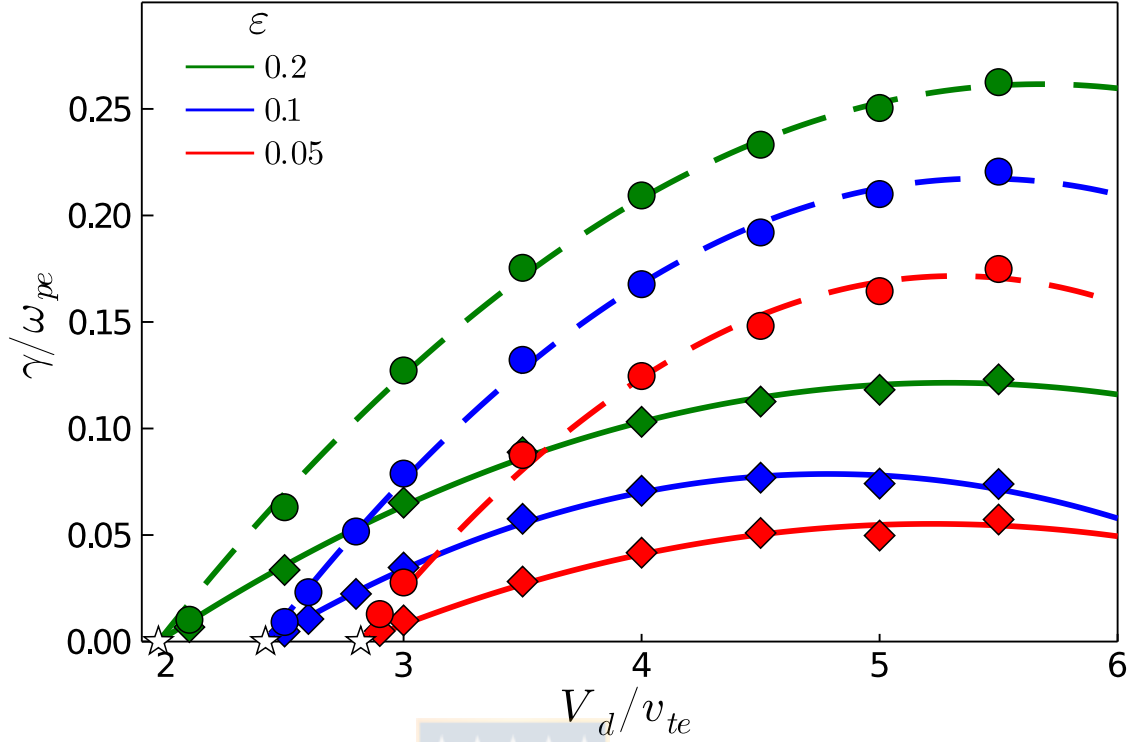


Figure 3.8: Transverse growth rates as a function of the relative drift velocity,  $V_d$ , for simulations with  $\varepsilon = 0.05$  (red),  $\varepsilon = 0.1$  (blue), and  $\varepsilon = 0.2$  (green). Diamonds mark the maximum transverse growth rate,  $\gamma_m$ , measured for oblique modes with parallel wavenumber  $k_0$ , after the nonlinear saturation of the perturbed mode  $(k_0, 0)$ . Solid lines are quadratic fits: in red  $\gamma(V_d) = 0.046(V_d - V_{th}^{\varepsilon=0.05}) - 0.01(V_d - V_{th}^{\varepsilon=0.05})^2$ , in blue  $\gamma(V_d) = 0.067(V_d - V_{th}^{\varepsilon=0.1}) - 0.014(V_d - V_{th}^{\varepsilon=0.1})^2$ , and in green  $\gamma(V_d) = 0.073(V_d - V_{th}^{\varepsilon=0.2}) - 0.011(V_d - V_{th}^{\varepsilon=0.2})^2$ . Circles mark the growth rate of the same modes during the linear stage, obtained from linear theory, and the dashed lines are quadratic fits. Stars on the horizontal axis mark the linear instability thresholds,  $V_{th}^{\varepsilon=0.05}/v_{te} = 2.82$ ,  $V_{th}^{\varepsilon=0.1}/v_{te} = 1.97$ , and  $V_{th}^{\varepsilon=0.2}/v_{te} = 2.42$  for the initial bump-on-tail configuration.

is dependant on the beam density. However, a clear change of behavior occurs in simulations with  $\varepsilon = 0.1$  (blue diamonds) for  $\gamma_L/\omega_{pe} \geq 0.2$  (or  $V_d/v_{te} \geq 4.5$ ). While



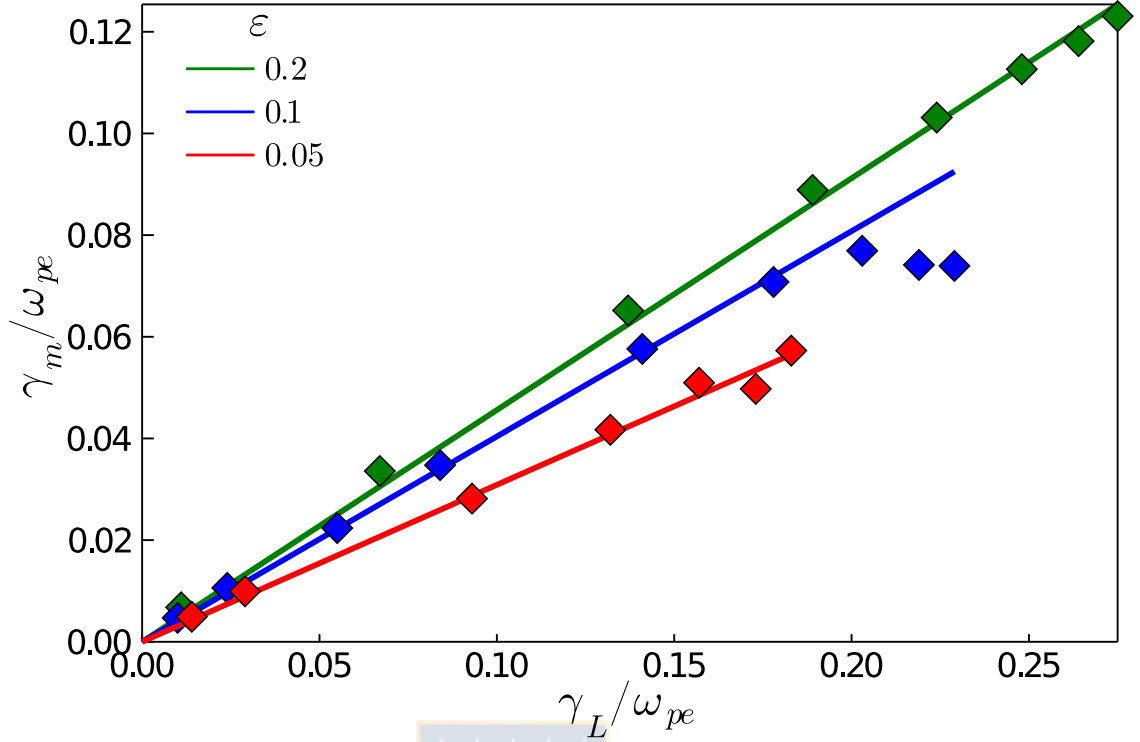


Figure 3.9: Maximum transverse growth rates,  $\gamma_m$ , as a function of the linear growth rate of the mode initially excited,  $\gamma_L$ , obtained from the linear dispersion relation. Each diamond is a different simulation. Red, blue and green colors mark configurations with  $\epsilon = 0.05$ ,  $\epsilon = 0.1$ , and  $\epsilon = 0.2$ , respectively. Solid lines are: in red  $\gamma_m^{\epsilon=0.05}(\gamma_L) = 0.309\gamma_L$ , in blue  $\gamma_m^{\epsilon=0.1}(\gamma_L) = 0.404\gamma_L$ , and in green  $\gamma_m^{\epsilon=0.2}(\gamma_L) = 0.456\gamma_L$ .

its explanation is not a part of the current work, the author is currently investigating the phenomenon.

Although the simulational data presented is not enough to uniquely identify the relation between the bump-on-tail instability and the transverse instability of the BGK-like modes formed, both instabilities were shown to be strongly correlated, sharing the same instability thresholds and having their growth rates connected through a simple proportionality relation, at least for drift velocities  $V_d/v_{te} \leq 4$ .

# Chapter 4

## Conclusions

A computational library to numerically solve the Vlasov-Poisson system of equations in 1 and 2 physical dimensions was successfully written, and it was employed to study the transverse instability of BGK-like modes self-consistently formed from bump-on-tail unstable distributions.

The simulations consisted mainly in 4 stages: (I) linear growth of wavevectors parallel and oblique to the beam, (II) formation of a BGK-like equilibrium from the most unstable beam-mode, parallel to the beam, with modification on the growth rate of the oblique modes, (III) saturation of the oblique modes and collapse of the BGK-like structure, and (IV) a nonlinear superposition of transverse harmonics of the BGK-like mode.

The linear dispersion relation was found to correctly predict the growth rates on stage I for 2-dimensional simulations.

The instability of a BGK-like mode towards perturbations transverse to its trapping direction was observed and described in detail. Oblique waves with the parallel wavenumber of the BGK-like mode are subject to exponential growth, and when they reach an amplitude comparable to that of the BGK-like mode, the latter collapses, losing a few orders of magnitude in energy. The thresholds for the transverse instability of BGK-like modes were shown to be coincident with the instability thresholds of

the initial bump-on-tail distributions, and the growth rates of both instabilities were shown to approximately follow a proportionality relation, at least for  $V_d/v_{te} < 4.5$ , supporting the hypothesis of work.

After the multi-dimensional collapse, transverse non-propagating waves of all sizes are excited, and the plasma evolves towards a state consisting on the nonlinear superposition of a continuous spectrum of transverse wavenumbers.

Vlasov-Poisson simulations have demonstrated to be a valuable tool to investigate the nature of the transverse instability of BGK-like modes. Future research includes the use of this kind of simulations to compare the transverse instability of self-consistently formed BGK-like modes, with the instability of similar structures, such as BGK-like modes formed by pumping of an external driver [12], and mathematical models currently in existence [11].



# Appendix A

## Conventions

Throughout this document, all mathematical expressions use the centimetre–gram–second (CGS) system of units, excepting for Sec. 2.3: Vlasov-Poisson Simulations, which uses normalized, dimensionless units.

### A.1 Characteristic quantities

When studying plasma physics, a common quantity to encounter is the *plasma frequency* of the species  $j$ ,

$$\omega_{pj} = \sqrt{\frac{4\pi n_j q_j^2}{m_j}}, \quad (\text{A.1})$$

which describes the characteristic frequency of a plasma composed of that species, where  $n_j$ ,  $q_j$  and  $m_j$  are the spatial density, charge and mass of the species  $j$ , respectively.

Another characteristic parameter is the *thermal speed* of the species  $j$ ,

$$v_{tj} = \sqrt{\frac{k_B T_j}{m_j}}, \quad (\text{A.2})$$

where  $T_j$  is the temperature of the species and  $k_B \approx 6.381[\text{erg} \cdot \text{K}^{-1}]$  is the Boltzmann's constant. Physically, the definition chosen for the thermal speed corresponds to the root mean square of the velocity of the particles along any single dimension.

One last quantity to define is the *Debye length* of the species  $j$ ,

$$\lambda_{Dj} = \sqrt{\frac{k_B T_j}{4\pi n_j q_j^2 + \sum_i \kappa_i n_i / T_i}}, \quad (\text{A.3})$$

where the index  $i$  is summed over all species present in the plasma, and  $\kappa_i$  is the ratio of the charges of the species  $i$  and  $j$ , respectively. The Debye length is the typical radius for an electric field to be screened by the plasma.

For an electron-proton plasma, it's usual to neglect the dynamics of the protons and approximate the Debye length as

$$\lambda_{De} = \sqrt{\frac{k_B T_e}{4\pi n_e q_e^2}}.$$

Note that, according to the definitions given,

$$v_{te} = \lambda_{De} \omega_{pe}.$$

## A.2 Gradient with respect to a vector

In general, for a given vector  $\mathbf{a} = a_x \hat{\mathbf{x}} + a_y \hat{\mathbf{y}} + a_z \hat{\mathbf{z}}$ , the expression

$$\frac{\partial}{\partial \mathbf{a}} = \hat{\mathbf{x}} \frac{\partial}{\partial a_x} + \hat{\mathbf{y}} \frac{\partial}{\partial a_y} + \hat{\mathbf{z}} \frac{\partial}{\partial a_z}$$

will be used to denote the gradient with respect to that vector. In this manner, if  $\mathbf{x}$  and  $\mathbf{v}$  are the usual position and velocity vectors, then  $\frac{\partial}{\partial \mathbf{x}}$  and  $\frac{\partial}{\partial \mathbf{v}}$  are the usual gradient and the velocity-gradient, respectively.

### A.3 Fourier transform

For a given function,  $g(x)$ , the definition of its Fourier transform,  $\widehat{g}(k)$ , will be given to follow relations

$$\begin{aligned}\widehat{g}(k) &= \mathcal{F}\{g\}(k) \\ &= \int_{\mathbb{R}} e^{-ikx} g(x) dx,\end{aligned}\tag{A.4a}$$

$$\begin{aligned}g(x) &= \mathcal{F}^{-1}\{\widehat{g}\}(x) \\ &= \frac{1}{2\pi} \int_{\mathbb{R}} e^{ikx} \widehat{g}(k) dk,\end{aligned}\tag{A.4b}$$

where  $k$  and  $x$  are conjugate variables.



# Appendix B

## Analytical Calculations

### B.1 Electrostatic dispersion relation for a Maxwellian equilibrium

Starting from the linear, electrostatic, dispersion relation,

$$1 + \sum_j \frac{\omega_{pj}^2}{k^2} \int_{\mathbb{R}^3} \frac{\mathbf{k}}{\omega - \mathbf{k} \cdot \mathbf{v}} \cdot \frac{\partial f_j^0}{\partial \mathbf{v}} d^3v = 0, \quad (\text{B.1})$$

we can consider a superposition of Maxwellian distributions of the form

$$f_j^0(\mathbf{v}) = \frac{1}{(2\pi)^{3/2} v_{tj}^3} \exp \left[ -\frac{(\mathbf{v} - \mathbf{V}_j)^2}{2v_{tj}^2} \right], \quad (\text{B.2})$$

where  $v_{tj}$  and  $\mathbf{V}_j$  are the thermal speed and the drift velocity of the species  $j$ , respectively.

It is always possible to express the velocities,  $\mathbf{v}$  and  $\mathbf{V}_j$ , in one component parallel and two components perpendicular to the perturbation wavevector,  $\mathbf{k}$ , such that

$$\begin{aligned} \mathbf{v} &= v^{\parallel} \hat{\mathbf{k}} + v^{\perp,1} (\hat{\mathbf{k}} \times \hat{\mathbf{v}}) + v^{\perp,2} (\hat{\mathbf{k}} \times \hat{\mathbf{k}} \times \hat{\mathbf{v}}), \\ \mathbf{V}_j &= V_j^{\parallel} \hat{\mathbf{k}} + V_j^{\perp,1} (\hat{\mathbf{k}} \times \hat{\mathbf{v}}) + V_j^{\perp,2} (\hat{\mathbf{k}} \times \hat{\mathbf{k}} \times \hat{\mathbf{v}}), \end{aligned}$$

where  $\hat{\mathbf{k}}$  and  $\hat{\mathbf{v}}$  are unitary vectors pointing in the direction of  $\mathbf{k}$  and  $\mathbf{v}$ , respectively. Then, the integral term in eq. (B.1) can be rewritten as

$$\begin{aligned} \int_{\mathbb{R}^3} \frac{\mathbf{k}}{\omega - \mathbf{k} \cdot \mathbf{v}} \cdot \frac{\partial f_j^0}{\partial \mathbf{v}} d^3v &= \frac{1}{(2\pi)^{3/2} v_{tj}^3} \int_{\mathbb{R}} \frac{k}{\omega - kv^{\parallel}} \frac{\partial}{\partial v^{\parallel}} \exp \left[ -\frac{(v^{\parallel} - V_j^{\parallel})^2}{2v_{tj}^2} \right] dv^{\parallel} \\ &\quad \times \int_{\mathbb{R}} \exp \left[ -\frac{(v^{\perp,1} - V_j^{\perp,1})^2}{2v_{tj}^2} \right] dv^{\perp,1} \\ &\quad \times \int_{\mathbb{R}} \exp \left[ -\frac{(v^{\perp,2} - V_j^{\perp,2})^2}{2v_{tj}^2} \right] dv^{\perp,2}, \end{aligned}$$

but since  $\int_{\mathbb{R}} \exp[-(v - a)^2/2b^2] dv = |b|\sqrt{2\pi}$  for  $b \in \mathbb{R}$ , then

$$\begin{aligned} \int_{\mathbb{R}^3} \frac{\mathbf{k}}{\omega - \mathbf{k} \cdot \mathbf{v}} \cdot \frac{\partial f_j^0}{\partial \mathbf{v}} d^3v &= \frac{1}{\sqrt{2\pi} v_{tj}} \int_{\mathbb{R}} \frac{k}{\omega - kv^{\parallel}} \frac{\partial}{\partial v^{\parallel}} \exp \left[ -\frac{(v^{\parallel} - V_j^{\parallel})^2}{2v_{tj}^2} \right] dv^{\parallel} \\ &= -\frac{1}{\sqrt{2\pi} v_{tj}^3} \int_{\mathbb{R}} \frac{k(v^{\parallel} - V_j^{\parallel})}{\omega - kv^{\parallel}} \exp \left[ -\frac{(v^{\parallel} - V_j^{\parallel})^2}{2v_{tj}^2} \right] dv^{\parallel}. \end{aligned}$$

Changing the integration variable to  $t = (v^{\parallel} - V_j^{\parallel})/\sqrt{2}v_{tj}$

$$\begin{aligned} \int_{\mathbb{R}^3} \frac{\mathbf{k}}{\omega - \mathbf{k} \cdot \mathbf{v}} \cdot \frac{\partial f_j^0}{\partial \mathbf{v}} d^3v &= \frac{1}{\sqrt{2\pi} v_{tj}^3} \int_{\mathbb{R}} \frac{2ktv_{tj}^2}{\omega - kV_j^{\parallel} - \sqrt{2}ktv_{tj}} \exp(-t^2) dt, \\ &= -\frac{1}{\sqrt{\pi} v_{tj}^2} \int_{\mathbb{R}} \frac{t}{(\omega - kV_j^{\parallel})/\sqrt{2}kv_{tj} - t} \exp(-t^2) dt, \end{aligned}$$

and defining the resonance factor,  $\xi = (\omega - \mathbf{k} \cdot \mathbf{V}_j) / \sqrt{2}kv_{tj}$ , integrating by parts, and using  $\partial(t - \xi)^{-1}/\partial\xi = (\xi - t)^{-2}$ , respectively, it is easy to see that

$$\begin{aligned} \int_{\mathbb{R}^3} \frac{\mathbf{k}}{\omega - \mathbf{k} \cdot \mathbf{v}} \cdot \frac{\partial f_j^0}{\partial \mathbf{v}} d^3v &= -\frac{1}{\sqrt{\pi} v_{tj}^2} \int_{\mathbb{R}} \frac{t}{\xi - t} \exp(-t^2) dt, \\ &= \frac{1}{2\sqrt{\pi} v_{tj}^2} \int_{\mathbb{R}} \frac{\exp(-t^2)}{(\xi - t)^2} dt, \\ &= \frac{1}{2v_{tj}^2} \frac{\partial}{\partial \xi} \left( \frac{1}{\sqrt{\pi}} \int_{\mathbb{R}} \frac{\exp(-t^2)}{t - \xi} dt \right), \end{aligned}$$

where the term in parenthesis is the plasma dispersion function,  $Z(\xi)$ .



Combining the last expression with eq. (B.1), the linear, electrostatic, dispersion relation for an equilibrium made up from a superposition of Maxwellian distributions is found to be

$$1 + \sum_j \frac{\omega_{pj}^2}{2v_{tj}^2 |\mathbf{k}|^2} Z' \left( \frac{\omega - \mathbf{k} \cdot \mathbf{V}_j}{\sqrt{2} v_{tj} |\mathbf{k}|} \right) = 0. \quad (\text{B.3})$$

(Ref. from 1 on page 9)



# Bibliography

- [1] I. Bernstein, J. Greene, and M. Kruskal. “Exact nonlinear plasma oscillations”. In: *Physical Review* 108.3 (1957), pp. 546–550. DOI: 10.1103/PhysRev.108.546 (cit. on pp. 1, 3, 15).
- [2] R. Ergun *et al.* “Debye-scale plasma structures associated with magnetic-field-aligned electric fields”. In: *Physical Review Letters* (1998). DOI: 10.1103/PhysRevLett.81.826 (cit. on pp. 1, 3, 16).
- [3] K. Saeki *et al.* “Formation and Coalescence of Electron Solitary Holes”. In: *Phys. Rev. Lett.* 42 (8 Feb. 1979), pp. 501–504. DOI: 10.1103/PhysRevLett.42.501 (cit. on pp. 1, 3, 16).
- [4] M. Shoucri. “Nonlinear evolution of the bump-on-tail instability”. In: *Physics of Fluids* 22.10 (1979), pp. 2038–2039. DOI: 10.1063/1.862470 (cit. on pp. 1, 3, 16).
- [5] L. Demeio and P. Zweifel. “Numerical simulations of perturbed Vlasov equilibria”. In: *Physics of Fluids B* (1990). DOI: 10.1063/1.859265 (cit. on pp. 1, 3, 16).
- [6] I. Hutchinson. “Electron holes in phase space: What they are and why they matter”. In: *Physics of Plasmas* 24.5 (2017). DOI: 10.1063/1.4976854 (cit. on pp. 1, 3, 16, 17).

- [7] R. Morse and C. Nielson. “One-, two-, and three-dimensional numerical simulation of two-Beam plasmas”. In: *Physical Review Letters* 23.19 (1969), pp. 1087–1090. DOI: 10.1103/PhysRevLett.23.1087 (cit. on pp. 1, 3, 17).
- [8] H. Rose and L. Yin. “Langmuir wave filamentation instability”. In: *Physics of Plasmas* 15.4 (2008), pp. 1–26. DOI: 10.1063/1.2901197 (cit. on pp. 1, 3, 17).
- [9] R. Berger *et al.* “Multi-dimensional Vlasov simulations and modeling of trapped-electron-driven filamentation of electron plasma waves”. In: *Physics of Plasmas* 22.5 (2015). DOI: 10.1063/1.4917482 (cit. on pp. 1–4).
- [10] L. Yin *et al.* “Saturation of backward stimulated scattering of laser in kinetic regime: Wavefront bowing, trapped particle modulational instability, and trapped particle self-focusing of plasma waves”. In: *Physics of Plasmas* 15.1 (2008). DOI: 10.1063/1.2825663 (cit. on pp. 1, 3, 17).
- [11] Denis A. Silantyev, Pavel M. Lushnikov, and Harvey A. Rose. “Langmuir wave filamentation in the kinetic regime. I. Filamentation instability of Bernstein-Greene-Kruskal modes in multidimensional Vlasov simulations”. In: *Physics of Plasmas* 24.4 (2017), p. 042104. DOI: 10.1063/1.4979289 (cit. on pp. 1–4, 17, 30, 44).
- [12] T. Chapman *et al.* “Longitudinal and Transverse Instability of Ion Acoustic Waves”. In: *Physical Review Letters* 119.5 (2017), pp. 1–5. DOI: 10.1103/PhysRevLett.119.055002 (cit. on pp. 1, 3, 17, 44).
- [13] J. Bezanson *et al.* “Julia: A fresh approach to numerical computing”. In: *SIAM review* 59.1 (2017), pp. 65–98. DOI: 10.1137/141000671 (cit. on pp. 5, 20).
- [14] A. Vlasov. “The vibrational properties of an electron gas”. In: *Physics-Usp ekhi* 721 (1968). DOI: 10.1070/PU1968v010n06ABEH003709 (cit. on pp. 7, 9).
- [15] R. Davidson. “Kinetic waves and instabilities in a uniform plasma”. In: *Handbook of Plasma Physics, Vol 1: Basic Plasma Physics* (1983), pp. 519–585 (cit. on p. 8).

- [16] L. Landau. “On the vibrations of the electronic plasma”. In: *J. Phys. (USSR)* 10 (1946), pp. 25–34. DOI: 10.1016/B978-0-08-010586-4.50066-3 (cit. on pp. 9, 10).
- [17] B. Fried and S. Conte. “The Plasma Dispersion Function: The Hilbert Transform of the Gaussian”. In: *Mathematics of Computation* (1963). DOI: 10.2307/2003748 (cit. on p. 9).
- [18] S. Ichimaru. *Statistical Plasma Physics*. Vol. 1. 1991. ISBN: 0-201-55490-9 (cit. on p. 12).
- [19] L. Muschietti *et al.* “Transverse instability of magnetized electron holes”. In: *Physical Review Letters* 85.1 (2000), pp. 94–97. DOI: 10.1103/PhysRevLett.85.94 (cit. on p. 17).
- [20] I. Hutchinson. “Kinematic Mechanism of Plasma Electron Hole Transverse Instability”. In: *Phys. Rev. Lett.* 120 (20 2018), p. 205101. DOI: 10.1103/PhysRevLett.120.205101 (cit. on p. 17).
- [21] R. Courant, K. Friedrichs, and H. Lewy. “On the Partial Difference Equations of Mathematical Physics”. In: *IBM Journal of Research and Development* 11.2 (1967), pp. 215–234. DOI: 10.1147/rd.112.0215 (cit. on p. 18).
- [22] R. Courant, E. Isaacson, and M. Rees. “On the solution of nonlinear hyperbolic differential equations by finite differences”. In: *Communications on Pure and Applied Mathematics* (1952). DOI: 10.1002/cpa.3160050303 (cit. on p. 19).
- [23] C. Cheng and G. Knorr. “The integration of the vlasov equation in configuration space”. In: *Journal of Computational Physics* 22.3 (1976), pp. 330–351. DOI: 0.1016/0021-9991(76)90053-X (cit. on pp. 19, 20, 24).
- [24] O. Pezzi, E. Camporeale, and F. Valentini. “Collisional effects on the numerical recurrence in Vlasov-Poisson simulations”. In: *Physics of Plasmas* 23.2 (2016). DOI: 10.1063/1.4940963 (cit. on p. 20).

- [25] L. Einkemmer and A. Ostermann. “A strategy to suppress recurrence in grid-based Vlasov solvers”. In: *European Physical Journal D* 68.7 (2014). DOI: 10.1140/epjd/e2014-50058-x (cit. on p. 20).
- [26] A. Klimas and A. Viñas. “Absence of Recurrence in Fourier-Fourier Transformed Vlasov-Poisson Simulations”. In: 1 (2018). DOI: 10.1017/S0022377818000776 (cit. on p. 20).
- [27] Y. Barsamian *et al.* “Verification of 2D x 2D and Two-Species Vlasov-Poisson Solvers”. In: *ESAIM: Proceedings and Surveys* (2018). DOI: 10.1051/proc/201863078 (cit. on p. 20).
- [28] H. Yoshida. “Symplectic Integrators for Hamiltonian Systems: Basic Theory”. In: *Symposium - International Astronomical Union* 152 (1992), pp. 407–411. DOI: 10.1017/S0074180900091440 (cit. on p. 22).
- [29] G. Strang. “On the Construction and Comparison of Difference Schemes”. In: *SIAM Journal on Numerical Analysis* (1968). DOI: 10.1137/0705041 (cit. on p. 22).
- [30] C. Swope *et al.* “A computer simulation method for the calculation of equilibrium constants for the formation of physical clusters of molecules: Application to small water clusters”. In: *The Journal of Chemical Physics* 76.1 (1982), pp. 637–649. DOI: 10.1063/1.442716 (cit. on p. 23).
- [31] H. Yoshida. “Construction of higher order symplectic integrators”. In: *Physics Letters A* 150.5-7 (1990), pp. 262–268. DOI: 10.1016/0375-9601(90)90092-3 (cit. on p. 24).
- [32] S. Chin. “Symplectic integrators from composite operator factorizations”. In: *Physics Letters, Section A: General, Atomic and Solid State Physics* 226.6 (1997), pp. 344–348. DOI: 10.1016/S0375-9601(97)00003-0 (cit. on p. 24).

- [33] M. Shoucri. “Destruction of trapping oscillations by sideband instability”. In: *Physics of Fluids* 23.10 (1980), pp. 2030–2033. DOI: 10.1063/1.862889 (cit. on p. 30).
- [34] M. Brunetti, F. Califano, and F. Pegoraro. “Asymptotic evolution of nonlinear Landau damping”. In: *Physical Review E - Statistical Physics, Plasmas, Fluids, and Related Interdisciplinary Topics* 62.3 B (2000), pp. 4109–4114. DOI: 10.1103/PhysRevE.62.4109 (cit. on p. 30).

